Mars Entry Atmospheric Data System Trajectory Reconstruction Algorithms and Flight Results

Christopher D. Karlgaard[*], Prasad Kutty[†]

Analytical Mechanics Associates, Inc., Hampton, VA

Mark Schoenenberger[‡]

NASA Langley Research Center, Hampton, VA

Jeremy Shidner[§]

Binera, Inc., Hampton, VA

Michelle Munk[¶]

NASA Langley Research Center, Hampton, VA

The Mars Entry Atmospheric Data System is a part of the Mars Science Laboratory, Entry, Descent, and Landing Instrumentation project. These sensors are a system of seven pressure transducers linked to ports on the entry vehicle forebody to record the pressure distribution during atmospheric entry. These measured surface pressures are used to generate estimates of atmospheric quantities based on modeled surface pressure distributions. Specifically, angle of attack, angle of sideslip, dynamic pressure, Mach number, and freestream atmospheric properties are reconstructed from the measured pressures. Such data allows for the aerodynamics to become decoupled from the assumed atmospheric properties, allowing for enhanced trajectory reconstruction and performance analysis as well as an aerodynamic reconstruction, which has not been possible in past Mars entry reconstructions. This paper provides details of the data processing algorithms that are utilized for this purpose. The data processing algorithms include two approaches that have commonly been utilized in past planetary entry trajectory reconstruction, and a new approach for this application that makes use of the pressure measurements. The paper describes assessments of data quality and preprocessing, and results of the flight data reduction from atmospheric entry, which occurred on August 5th, 2012.

I.   Introduction

On August 5th 2012, the Mars Science Laboratory (MSL)[1] entry vehicle (EV) successfully entered the Mars atmosphere and landed the Curiosity rover safely on the surface of the planet in Gale crater. MSL carried with it a unique instrumentation package designed to measure the aerodynamic and aerothermal environments during atmospheric entry. This instrumentation package is known as the MSL Entry, Descent, and Landing Instrumentation (MEDLI),[2] which consists of two major subsystems, the Mars Entry Atmospheric Data System (MEADS) and the MEDLI Integrated Sensor Plugs (MISP). The MEADS consists of seven pressure transducers connected to flush orifices in the heat shield forebody to measure the pressure distribution. The MISP devices are a system of thermocouple and recession sensors to provide aerothermal

---

[*]Supervising Engineer, Senior Member AIAA.

[†]Project Engineer.

[‡]Aerospace Engineer, Atmospheric Flight and Entry Systems Branch.

[§]Senior Project Engineer, Senior Member AIAA.

[¶]MEADS System Lead, Atmospheric Flight and Entry Systems Branch.

measurements of the heat shield performance. The MEDLI sensors provide key measurements that can be used for trajectory reconstruction and engineering validation of aerodynamic, atmospheric, and thermal protection system models in addition to Earth-based systems testing procedures. Such validation directly benefits future planetary entry, descent, and landing (EDL) by reducing uncertainties associated with these models and procedures.

The basic MEADS science objectives are to reconstruct atmospheric data variables from pressure measurements alone when the free stream dynamic pressure is above 850 Pa. In particular, the objectives are to estimate the angles of attack and sideslip to within 0.5 deg and the dynamic pressure to within 2%, in a 3σ sense. Secondary objectives are to estimate the Mach number, freestream density and atmospheric winds from the MEADS pressure measurements, when combined with the on-board Inertial Measurement Unit (IMU) data. These measurements serve to enhance the MSL trajectory reconstruction and performance analysis, and enable a separation of the aerodynamics from the atmosphere, which prior to MEADS has not been achievable for Mars EDL reconstruction. The concept is an implementation of the Flush Air Data System (FADS).

The concept of the Flush Air Data System (FADS) was conceived and developed specifically to provide research quality air data during the hypersonic flight regime where the classical Pitot static probe could not survive. While limited hypersonic air data was acquired during the X-15 program using a servoed Q-Ball Air Data System (see References 3 and 4), such a concept is not compatible with blunt entry configurations. A blunt-body FADS was attempted on the Viking 1 and 2 entry vehicles, with limited success.[5] The initial flight FADS was proposed and developed under the Orbiter Experiments Program as the Shuttle Entry Air Data System (SEADS), documented in References 6–22. The Space Shuttle Orbiter provides a model for the accomplishment of a staged program for verifying EDL technology readiness. In addition to an elaborate ground test program and sub-scale flight testing, the initial manned full scale testing was accomplished using full scale un-powered final approach and landing tests. To support the reentry flight, an expanded data acquisition program was defined for the initial orbital flights of the Orbiter. These flights were flown on relatively low risk entry trajectories while EDL data was collected by the Development Flight Instrumentation (DFI). These first five development flights were specifically designed to collect the EDL data required to expand the flight envelope as uncertainties were addressed and reduced. The data was oriented towards the validation of structural loads, heat loads and GN&C uncertainties. The data from these flights significantly impacted the orbiter EDL operations. As the design and development of SEADS hardware and data reduction software evolved the system's objective expanded to demonstrate the concept as one with an across the speed range air data capability - subsonic through hypersonic and ascent. SEADS successfully flew five research/demonstration of concept missions on the orbiter OV-102 (Columbia). This development and flight success of SEADS clearly demonstrates the applicability of the FADS concept to blunt entry vehicles across the speed range. Through proper design, implementation and calibration an air data system based on the FADS concept can provide highly accurate air data to accomplish entry technology research and/or active flight control.

Subsequent to the introduction of the FADS concept for the Shuttle Orbiter, the FADS concept has been recommended and/or considered and/or utilized to acquire air data on many flight systems including high performance aircraft[23,24] (B-2, F-14, F-18, F-22), guided munitions,[25] and entry/hypersonic systems with various degrees of bluntness. These systems include the blunt Aeroassist Flight Experiment (AFE)[26,27] and Pathfinder (which was not manifested) and higher fineness ratio vehicles including HYFLITE, HYFLEX, X-31, X-33, X-34, X-37, and X-43. FADS was recently utilized on the Orion Pad Abort One flight test, and will also be implemented on the Exploration Flight Test One. References 28–37 provide additional details as to the implementation of FADS concepts for these various applications. The flights of the SEADS and the design and development work accomplished in support of the AFE FADS have a heritage that closely relates to the MSL configuration. This background, coupled with the demonstrated flexibility of the FADS concept adequately demonstrates the desirability and the applicability of FADS to MSL.

The MEDLI/MEADS project installed seven pressure ports through the MSL PICA heat shield at strategic locations to acquire heat shield surface pressure data during the atmospheric entry phase at Mars. The MEADS pressure ports are located on the MSL heat shield as shown in Figure 1(a). The PICA tile layout is also shown in this figure along with the predicted flow streamlines over the surface of the Thermal Protection System (TPS). All of the pressure ports are located a minimum of 3-inches from the PICA tile seams. At each of the pressure port locations there is an independent pressure measurement system installed on the internal surface of the heat shield support structure.

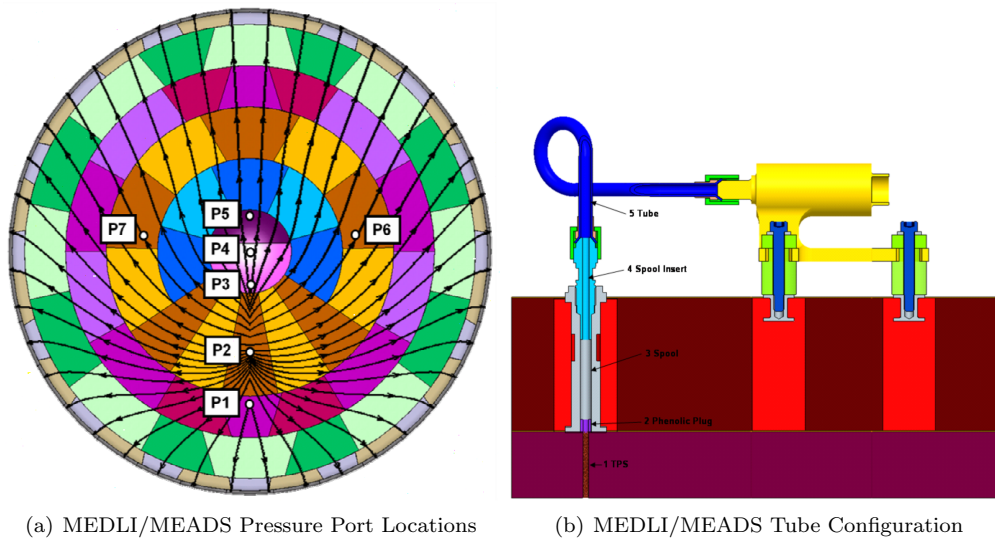(a) MEDLI/MEADS Pressure Port Locations   (b) MEDLI/MEADS Tube Configuration

Figure 1: MEDLI/MEADS Geometry

Pressure ports P1 and P2 are located in the stagnation region to provide a nearly direct measurement of the total pressure at the high Mach regime. Ports P3, P4, and P5 lie on the spherical cap and are placed in order to take advantage of the simple geometry for angle of attack measurements. Additionally, P4, located at the geometric center, provides a nearly direct total pressure measurement at the low Mach regime prior to parachute deployment. The final two ports are located in the horizontal plane of symmetry, approximately 1.0 meters off of the centerline. The ports P6 and P7 provide the off-axis measurements needed to estimate the angle of sideslip. The pressure ports are connected to pressure transducers via a tube system illustrated in Figure 1(b). The measured pressures are sampled at a rate of 8 Hz during entry.

This paper provides an overview of the data processing algorithms utilized for MSL/MEADS trajectory reconstruction and the results of the reconstruction. These techniques consist of three semi-independent methods that utilize different portions of the entire data set. An overview of the raw data is provided, along with an assessment of data quality and comparison with simulation results. Techniques used to preprocess the data are described, which includes editing out suspect data and smoothing to reduce noise. The MISP sensors and associated modeling and reconstruction techniques are documented in Refs. 38–40 and are not discussed further in this paper.

The remainder of the paper is organized as follows. Section II provides an overiview of the EDL timeline. Section III discusses the trajectory estimation techniques that have been implemented for MSL trajectory reconstruction. EDL data processing and trajectory reconstruction results are described in Section IV, and conclusions are provided in Section V.

II.   Mars Science Laboratory Entry, Descent, and Landing Overview

Figure 2 shows a timeline of the different EDL events.[41] Note that the event times correspond to the nominal trajectory. Actual times differed from the nominal event times due to dispersions in the entry time and atmospheric uncertainties. EDL consists of six major segments: Exo-Atmospheric, Entry, Parachute Descent, Powered Descent, Sky Crane, and Fly Away.[42] The Exo-Atmospheric segment begins once the cruise stage separation command is sent. Once the cruise stage separates, Guidance, Navigation, and Control (GNC) is enabled. Once enabled, the entry body is despun and turned to its entry attitude. Then, the two 75-kg Cruise Balance Masses (CBMs) are jettisoned to enable aerodynamic lift.

The Entry segment starts with the vehicle at the Entry Interface Point (EIP) defined at 3522.2 km from the center of Mars, approximately 540 seconds after cruise stage separation. During the Entry segment, the vehicle goes through peak heating and peak deceleration, the Reaction Control System (RCS) controls the lift vector to achieve the desired down-range and cross-range target. Just prior to parachute deployment, six 25-kg Entry Balance Masses (EBMs) are jettisoned to eliminate lift and the vehicle rolls to point the

(a) Cruise Stage Separation to Parachute Deployment
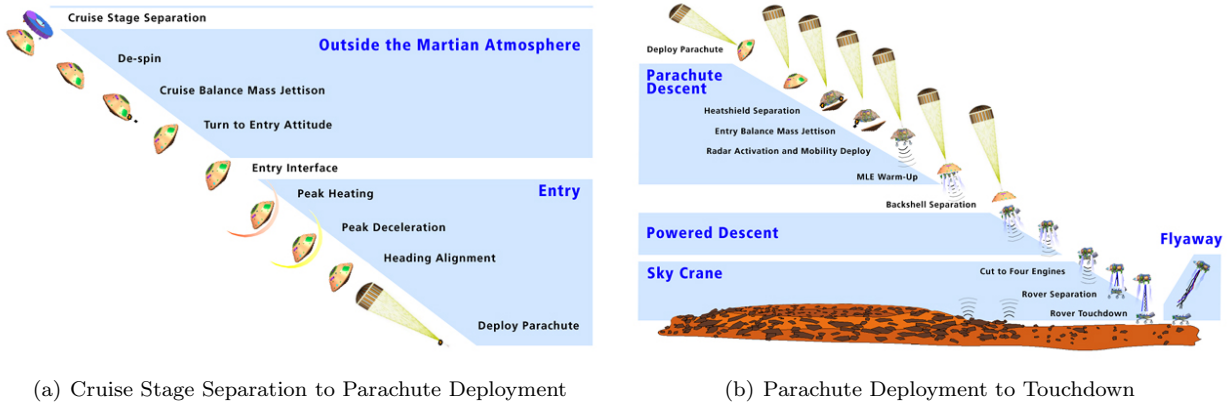

(b) Parachute Deployment to Touchdown

Figure 2: MSL Entry, Descent, and Landing

Terminal Descent Sensor (TDS) to the ground. This maneuver is called the Straighten Up and Fly Right maneuver (SUFR) or "Victory" roll. Figure 3 shows the nominal trajectory over the time period from entry interface to parachute deployment.

The Parachute descent segment starts with the parachute deployment triggered once the vehicle reached Mach 1.7. RCS wrist mode damping is active 10 s after parachute deployment to reduce wrist mode oscillations. Once the vehicle achieves a speed of Mach 0.7, the heat shield is jettisoned and the TDS starts acquiring the ground. Note that the MEDLI instruments are powered off 10 seconds prior to heat shield jettison. The command to jettison the backshell and the parachute is issued at an altitude of 1.6 km and at a velocity of approximately 79 m/s. Just before backshell separation, the Mars Landing Engines (MLEs) are primed in preparation for the start of the powered descent segment.

The Powered Descent segment begins at backshell separation. During powered descent, eight independently throttleable MLEs are actuated, initially to execute a divert maneuver for backshell avoidance which brings the vehicle to vertical flight at a descent rate of 32 m/s. Once vertical flight is achieved, a descent at constant velocity to adjust for altitude error at backshell separation starts. This constant velocity phase is followed by a constant deceleration phase, which reducs the vehicle's speed to 0.75 m/s in preparation for the sky crane segment. At this time, the four inboard MLEs are throttled down to near shutdown (1%) while the four remaining MLEs were throttled at 50%.

The Sky Crane segment starts following issuance of the rover separation command, which occurrs at an altitude of approximately 18.6 m. The rover is lowered to 7.5 m below the descent stage. Then, the descent stage continues to descend until post-touchdown is detected.

The Fly Away segment starts after touchdown is sensed. Once the descent stage stops it's vertical motion, the bridle and electrical umbilical devices are cut and two of the MLE engines are throttled up to 100% while the other two engines are at slightly less than 100%. This causes the descent stage to pitch to 45 degrees. Once the turn maneuver is completed, all four engines are throttled up to 100%. Constant thrust is applied to ensure the descent stage impacts the surface at least 300 m from the landing point.

III.   Trajectory Reconstruction Methods

This section provides a detailed description of various trajectory reconstruction methods that have been implemented for MSL EDL reconstruction. These reconstruction methods include three semi-independent methods that each make use of a different set of data for the reconstruction. The three semi-independent methods include an inertial reconstruction, that makes use of IMU measured accelerations and rates alone; an approach based on the vehicle aerodynamic database and sensed acceleration measurements; and a method based on the surface pressure measurements from the MEADS transducers. The first two of these methods have historically been the primary approaches to EDL reconstructions, for examples see References 43–48. The third method based on the surface pressure measurements has heritage from the SEADS program, but is new for this application to Mars EDL reconstruction. One key difference between the SEADS and MEADS pressure algorithms is that the SEADS pressure models were based on modified Newtonian theory, calibrated

American Institute of Aeronautics and Astronautics

(a) Altitude

(b) Mach

(c) Dynamic Pressure

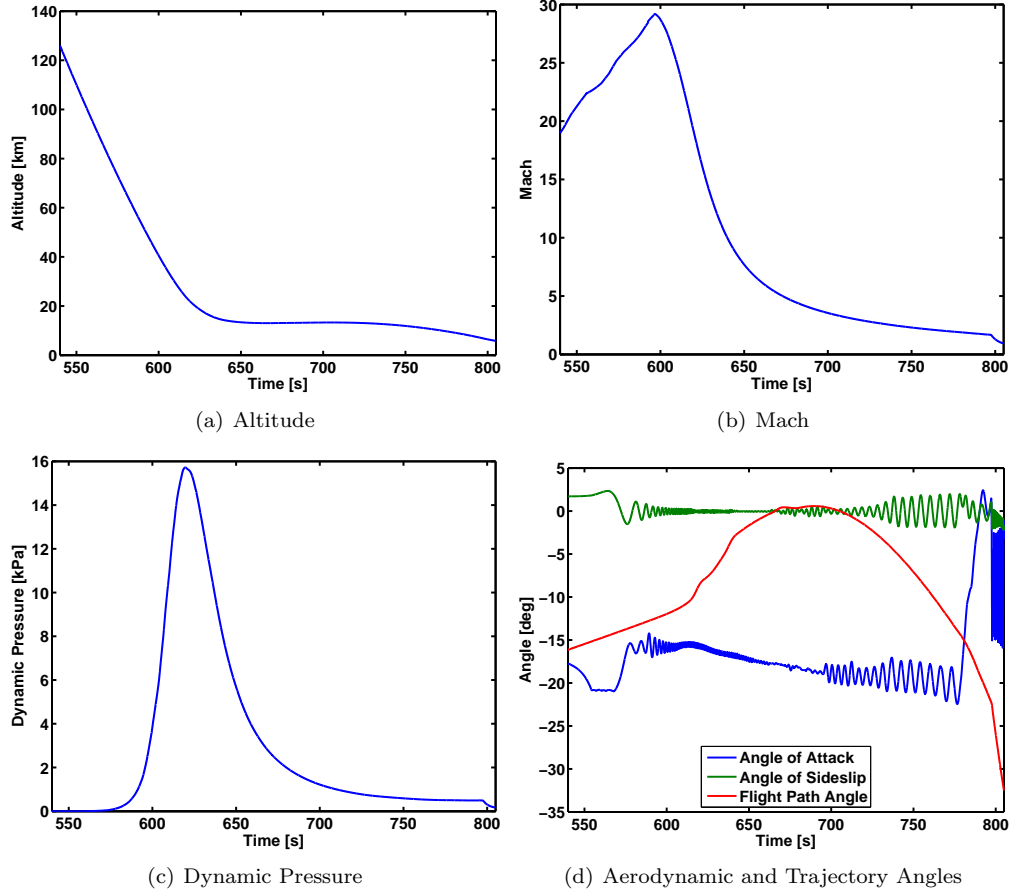(d) Aerodynamic and Trajectory Angles

Figure 3: MSL Nominal Trajectory: Entry Interface to Heatshield Separation

to wind tunnel experiments, whereas the MEADS pressure models are based entirely on CFD solutions. The following subsections provide details on each of the reconstruction approaches.

A. Inertial Reconstruction

The IMU-based reconstruction algorithm implemented for MSL EDL reconstruction is based on direct numerical integration of the equations of motion, using initial conditions provided by orbit determination solutions and star tracker attitude updates prior to cruise stage separation. The equations of motion used in the reconstruction are based on Reference 49–53, listed below.

$$\dot{r} = -w \tag{1}$$

$$\dot{\phi} = \frac{u}{r} \tag{2}$$

$$\dot{\theta} = \frac{v}{r \cos \phi} - \Omega \tag{3}$$

$$
\left\{ \begin{array}{c} \dot{u} \\ \dot{v} \\ \dot{w} \end{array} \right\} = \boldsymbol{G}^T \left\{ \begin{array}{c} a_x \\ a_y \\ a_z \end{array} \right\} + \left\{ \begin{array}{c} \left(uw - v^2 \tan \phi\right)/r - \left(3\mu J_2/2r^4\right)\sin\left(2\phi\right) \\ \left(uv \tan \phi + vw\right)/r \\ -\left(u^2 + v^2\right)/r + \mu/r^2 - \left(3\mu J_2/2r^4\right)\left(2 - 3\cos^2 \phi\right) \end{array} \right\} \tag{4}
$$

$$
\left\{ \begin{array}{c} \dot{e}_0 \\ \dot{e}_1 \\ \dot{e}_2 \\ \dot{e}_3 \end{array} \right\} = \frac{1}{2} \left[\begin{array}{ccc} -e_1 & -e_2 & -e_3 \\ e_0 & -e_3 & e_2 \\ e_3 & e_0 & -e_1 \\ -e_2 & e_1 & e_0 \end{array} \right] \left(\left\{ \begin{array}{c} \omega_x \\ \omega_y \\ \omega_z \end{array} \right\} - \frac{1}{r} \boldsymbol{G} \left\{ \begin{array}{c} v \\ -u \\ -v \tan \phi \end{array} \right\} \right) \tag{5}
$$

where r is the radius of the vehicle from the center of the planet, θ is the longitude, ϕ is the declination, u, v, w are the inertial velocity components in a topocentric frame (defined by the z-axis direction along the radius vector, toward the center of the planet, and the y-axis to the east) e_i are the Euler parameters describing the attitude of the vehicle with respect to the topodetic frame (north-east-down). The quantity Ω is the planetary rotation rate.

The body axis sensed accelerations are transformed from the IMU location according to the relations

$$\left\{ \begin{array}{c} a_x \\ a_y \\ a_z \end{array} \right\} = \left\{ \begin{array}{c} \tilde{a}_x \\ \tilde{a}_y \\ \tilde{a}_z \end{array} \right\} - \left[\begin{array}{ccc} -\left(\omega_y^2 + \omega_z^2\right) & \left(\omega_x\omega_y - \dot{\omega}_z\right) & \left(\omega_x\omega_z + \dot{\omega}_y\right) \\ \left(\omega_x\omega_y + \dot{\omega}_z\right) & -\left(\omega_x^2 + \omega_z^2\right) & \left(\omega_y\omega_z - \dot{\omega}_x\right) \\ \left(\omega_x\omega_z - \dot{\omega}_y\right) & \left(\omega_y\omega_z + \dot{\omega}_x\right) & -\left(\omega_x^2 + \omega_y^2\right) \end{array} \right] \left\{ \begin{array}{c} x_m \\ y_m \\ z_m \end{array} \right\} \tag{6}$$

where $\tilde{a}_x$, $\tilde{a}_y$, and $\tilde{a}_z$ are the sensed accelerations at the IMU location, x_m, y_m and z_m are the position of the IMU with respect to the center of mass in the body frame, and ω_x, ω_y and ω_z are the body axis sensed angular velocity components.

These equations of motion are integrated using a fixed step 4th-order Runge-Kutta algorithm with integration rate of 200 Hz to match the rate of the MSL IMU data. Once integrated, the IMU reconstruction algorithm provides estimates of the planet relative trajectory based on the initial conditions and sensed accelerations and angular rates. Other quantities of interest, such as angle of attack, are computed from the integrated state variables during an output processing step. For IMU-only reconstruction, these outputs assume zero winds. An assumed atmosphere profile can be superimposed on the inertial trajectory in order to compute estimates of atmosphere-relative quantities such as dynamic pressure and Mach number.

B. Aerodatabase Reconstruction

This section provides a summary of the approach used to generate estimates of atmospheric relative parameters based on the vehicle aerodynamic database, combined with accelerometer measurements. The method implemented for MSL closely follows the approach taken with Mars Pathfinder, described in Reference 44. The method first reconstructs the atmospheric density and pressure profile, and then solves for the angles of attack and sideslip from ratios of sensed accelerations. The entire process is iterated until the estimates converge.
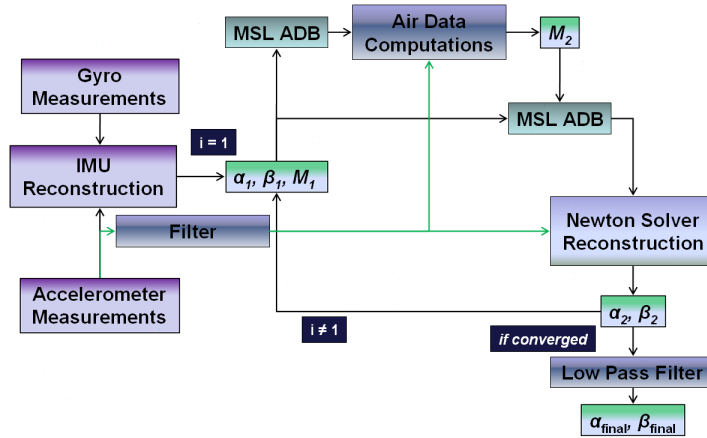

Figure 4: Aerodatabase Reconstruction Flow Diagram

The block diagram shown in Figure 4 presents a high level description of the aerodatabase reconstruction algorithm. The algorithm requires the use of two loops designed to converge on accurate estimates of angle of attack, angle of sideslip, Mach number, density, pressure, and temperature. The outer loop performs the calculations to generate the air data parameters using outputs from the MSL aerodynamic database. The inner loop exists inside of the Newton solver to update angle of attack and sideslip. Both loops rely on the aerodatabase, specifically for force coefficient outputs. The MSL aerodynamic database and associated uncertainties are described in Refs. 54 and 55.

The algorithm begins with an initial estimate of angle of attack, angle of sideslip, and Mach number. For the purposes of this application, an inertial reconstruction of these parameters is computed using the inertial

American Institute of Aeronautics and Astronautics

reconstruction method described in the previous section. During the first pass through the outer loop of the reconstruction algorithm, the MSL aerodatabase is called using the inertial inputs to generate an initial set of aerodynamic force and moment coefficients. The axial force coefficient is used to compute density. With this density estimate, pressure, speed of sound, Mach number, and temperature estimates can be computed.
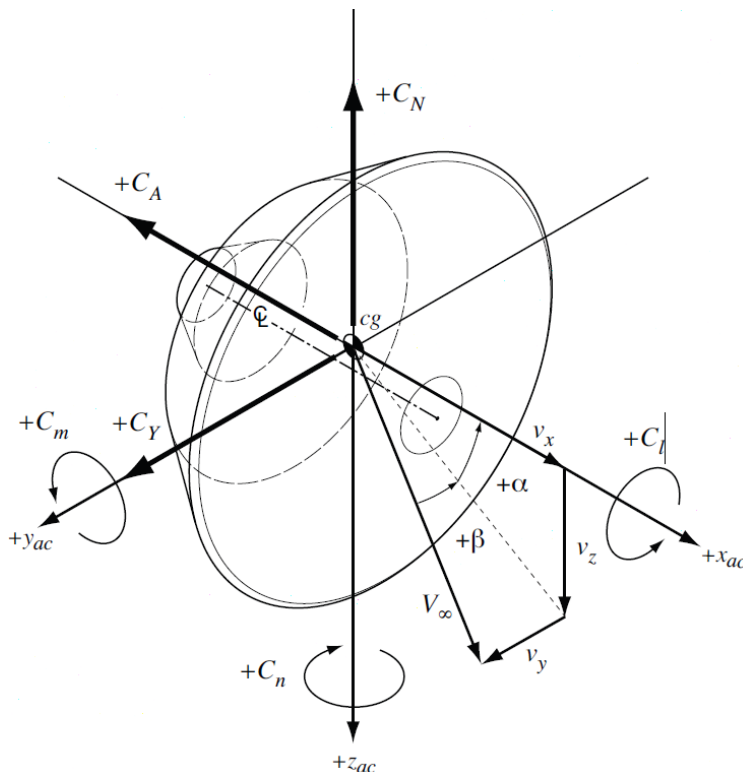

Figure 5: Aerodatabase Coordinate System

These updated air data states are used as inputs to the aerodatabase to produce an updated set of force and moment coefficients to begin the inner loop of the algorithm. The inner loop of the algorithm uses the Newton method to solve a system of non-linear equations, which are functions of angle of attack and sideslip, and are composed of the acceleration and force coefficient ratios. Newton's equation provides an update to angle of attack and sideslip using a numerically computed Jacobian matrix. The Newton solver is applied in a convergence loop that ends when the update to angle of attack and sideslip reaches a value smaller than the pre-defined threshold. (For this analysis, the convergence threshold was set to 10^{-6}). Once the loop ends, the updated angle of attack and sideslip are returned to the outer loop and used to query the aerodatabase in order to update the air data estimates. The outer loop and inner loop continue to run until both loops have converged. At this point, final estimates of angle of attack, angle of sideslip, pressure, density, speed of sound, Mach number and temperature have been reached. Mathematical details of the algorithm are as follows.

First, the density is computed from the measured axial force and predicted axial force coefficient from the aerodatabase by means of

$$\rho = \frac{2ma_x}{SC_A V^2} \tag{7}$$

where m is the vehicle mass, a_x is the axial acceleration of the vehicle at the center of mass, V is the atmospheric relative velocity, S is the vehicle reference area, and C_A is the axial force coefficient from the aerodatabase. Once the density is obtained, the pressure can be computed from numerical integration of the hydrostatic equation, which is given by $dp/dh_G = -\rho g$, where p is the static pressure, g is the gravitational acceleration, and h_G is the radial altitude. This equation can be integrated along the trajectory using an Euler discretization of the form

$$p_k = p_{k-1} - \rho_k g_k \left(h_{G_k} - h_{G_{k-1}} \right) \tag{8}$$

American Institute of Aeronautics and Astronautics

where k represents the time index. A simple gravity model can be used in the integration to compute acceleration as a function of altitude, given by

$$g = g_0 \left(\frac{R}{R + h_G} \right)^2 \tag{9}$$

where R is the planetary radius and g_0 is the reference gravitational acceleration at $h_G = 0$. Once the density and pressure are obtained, the Mach number can be computed using the relationship $M = V/\sqrt{\gamma p/\rho}$.

Next, the angles of attack and sideslip are computed based on ratios of accelerations combined with a Newton solver. The approach utilizes a comparison between the ratio of accelerations and the corresponding ratio of force coefficients. Ratios used for the estimation of the angles of attack and sideslip are given by

$$\frac{a_z}{a_x} = \frac{C_N}{C_A} \tag{10}$$

$$\frac{a_y}{a_x} = -\frac{C_Y}{C_A} \tag{11}$$

where a_x, a_y, and a_z are the body axis accelerations at the center of mass, and C_A, C_Y, and C_N are the axial, side, and normal force coefficients from the aerodatabase. These ratios can be rearranged to form

$$\boldsymbol{G}\left(\alpha, \beta\right) = \left\{ \begin{array}{c} g_1\left(\alpha, \beta\right) \\ g_2\left(\alpha, \beta\right) \end{array} \right\} = \left\{ \begin{array}{c} a_z/a_x - C_N/C_A \\ a_y/a_x + C_Y/C_A \end{array} \right\} = \left\{ \begin{array}{c} 0 \\ 0 \end{array} \right\} \tag{12}$$

Next, a root finding algorithm is applied to solve for the angle of attack and sideslip that satisfy Equation 12. For MSL reconstruction, a Newton method has been applied to solve Equation 12. The algorithm begins with an initial estimate of α and β based on the inertial reconstruction and then iterates until convergence using

$$\left\{ \begin{array}{c} \alpha_{i+1} \\ \beta_{i+1} \end{array} \right\} = \left\{ \begin{array}{c} \alpha_i \\ \beta_i \end{array} \right\} - \boldsymbol{J}\left(\alpha_i, \beta_i\right)^{-1} \boldsymbol{G}\left(\alpha_i, \beta_i\right) \tag{13}$$

where i denotes the iteration counter and $\boldsymbol{J}$ is the Jacobian matrix given by

$$\boldsymbol{J} = \left[\begin{array}{cc} \partial g_1/\partial \alpha & \partial g_1/\partial \beta \\ \partial g_2/\partial \alpha & \partial g_2/\partial \beta \end{array} \right] \tag{14}$$

which is evaluated numerically using perturbation values of 1 degree.

At each time point, the Newton solver must iterate until the roots converge upon the final estimate of angle of attack and sideslip. Convergence is determined to have occurred when the difference between two consecutive iterations of the algorithm has fallen below a desired tolerance or when a maximum number of iterations has occurred.

A key advantage of this reconstruction approach is that the estimates of the angles of attack and sideslip are wind-relative since the estimates are based on the aerodatabase. It is conceivable that the two different measures of the aerodynamic flow angles could be used to identify winds, in a manner similar that proposed in Reference 59; however, that approach suffers from a serious pitfall for the application to MSL so is not implemented here. The next section will elaborate further on issue of wind estimation.

C. Pressure-Based Reconstruction

The basic MEADS atmospheric state estimation procedure is essentially similar to the SEADS state estimation described in Reference 13, a point–wise least squares fit of the surface pressure measurements to the modeled pressure distribution to determine minimum–variance estimates of the atmospheric states. When combined with an Inertial Measurement Unit (IMU), the MEADS measurements can also be used to generate wind and density estimates. This section describes the techniques used to estimate these quantities, first providing details on the fore body surface pressure models and subsequently the basic MEADS estimation technique to compute the atmospheric state variables from the surface pressure measurements.
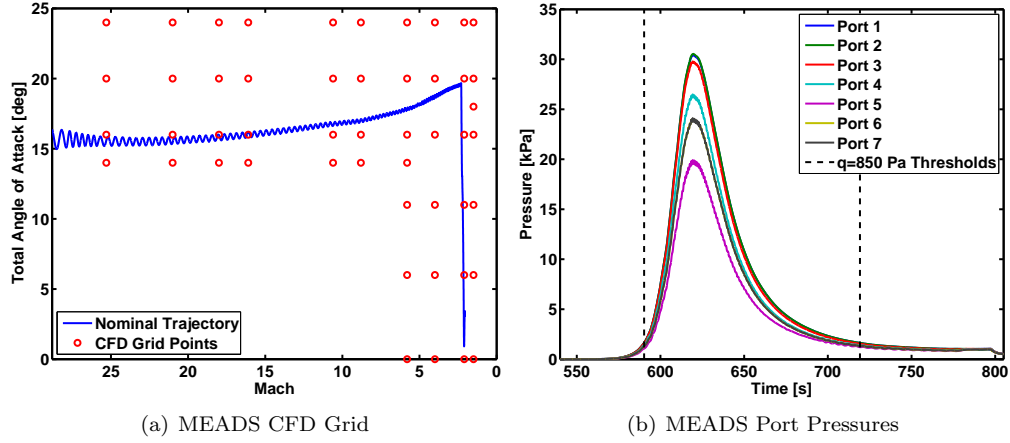
(a) MEADS CFD Grid

(b) MEADS Port Pressures

Figure 6: MEADS CFD Grid and Port Pressure

1. Pressure Modeling

A CFD-based table lookup model was developed for analysis of the MSL air data system. This CFD database is based on supersonic and hypersonic regime pressure distributions from thin–layer Navier–Stokes solutions generated using the Langley Aerothermal Upwind Relaxation Algorithm (LAURA). The relaxation of vibrational temperature of the CO_2 molecule is simulated using the Camac[56] model. Forebody solutions were obtained using a 7 block singularity-free grid.

The supplied CFD database was converted from absolute pressure to pressure coefficient in order to allow the pressure distribution to scale with different trajectories and to enable estimation of freestream atmospheric properties such as the static pressure. The data was re–interpolated from the 7 block grid to a single-zone grid of clock and cone angles. This alteration simplifies the interpolation of surface conditions without complications of search routines required to handle multiple zones.

The CFD grid points are shown as a function of total angle of attack and Mach number in Figure 6(a) along with the nominal reference trajectory. The pressure profiles for each MEADS port are shown in Figure 6(b). Note that each CFD grid point consists of a full surface pressure distribution solution, with 37 clock angles in uniform 5 deg increments and 61 cone angles with non-uniform increments. These grid points can be interpolated as needed to provide estimates of the pressure distribution at any point on the aeroshell.

2. Atmospheric State Estimation

By defining the atmospheric state vector as $\boldsymbol{x}$, where $\boldsymbol{x} = [\alpha, \beta, q, p_s]^T$, $\boldsymbol{p}$ is the vector of N observed surface pressures, and the CFD-based pressure model as $\boldsymbol{h}(\boldsymbol{x}, t)$, then the pressure measurement model can be written compactly as

$$\boldsymbol{p} = \boldsymbol{h}\left(\boldsymbol{x}, t_k\right) + \boldsymbol{\epsilon} \tag{15}$$

where $\boldsymbol{\epsilon}$ is the vector of pressure measurement errors and t_k is the measurement sampling time. The pressure measurement model can be approximated by means of the truncated series expansion

$$\boldsymbol{p} \approx \boldsymbol{h}\left(\bar{\boldsymbol{x}}, t_k\right) + \boldsymbol{H}(t_k)\left(\boldsymbol{x} - \bar{\boldsymbol{x}}\right) + \boldsymbol{\epsilon} \tag{16}$$

where $\bar{\boldsymbol{x}}$ is some reference state and $\boldsymbol{H}(t_k)$ is the Jacobian matrix

$$\boldsymbol{H}(t_k) = \left[\frac{\partial \boldsymbol{h}}{\partial \boldsymbol{x}}\right]_{\boldsymbol{x}=\bar{\boldsymbol{x}}} \tag{17}$$

which is also sometimes known as the measurement sensitivity matrix. The components of this matrix are shown in Figure 7 along the nominal trajectory. These sensitivities illustrate which ports provide the most information on a particular parameter, for instance the most leeward port 5 provides the most information

American Institute of Aeronautics and Astronautics

(a) $\partial \boldsymbol{p}/\partial \alpha$

(b) $\partial \boldsymbol{p}/\partial \beta$

(c) $\partial \boldsymbol{p}/\partial q$

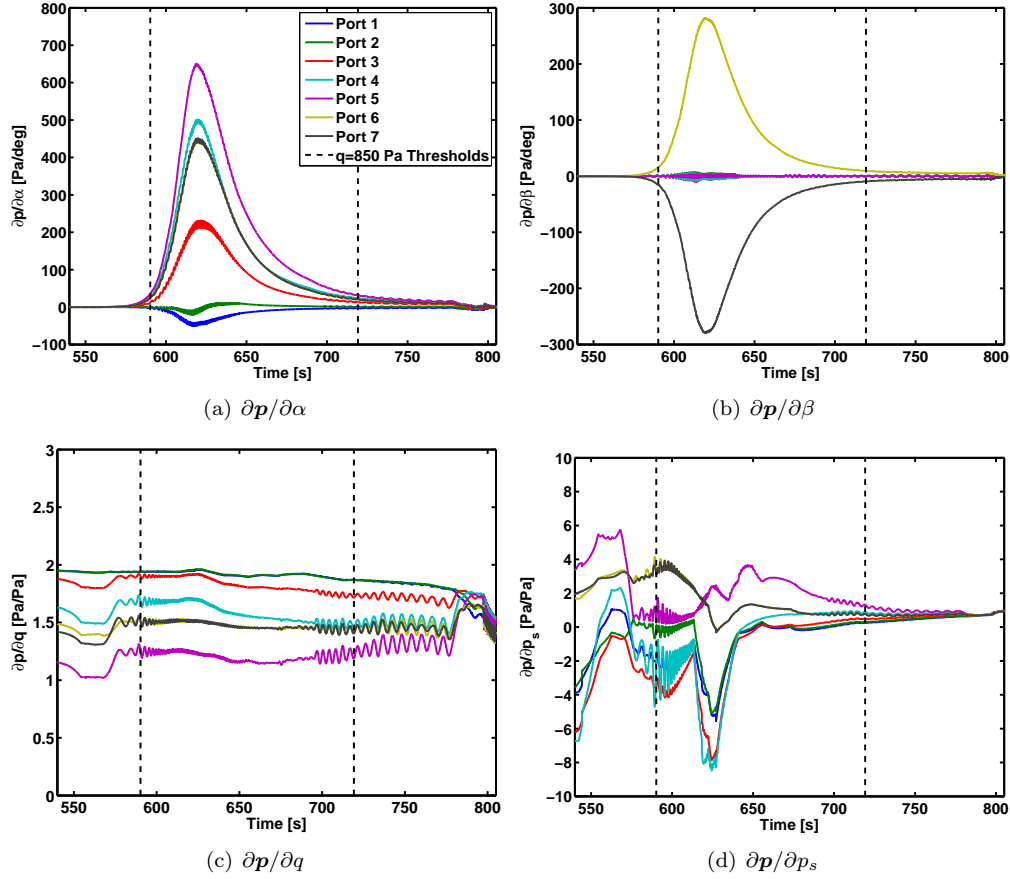(d) $\partial \boldsymbol{p}/\partial p_s$

Figure 7: Pressure Sensitivities

on the angle of attack, ports 6 and 7 provide the most information on sideslip, and ports 1 and 2 provide the most information on dynamic pressure.

The aerodynamic state estimation problem can be reduced to a linear regression problem of the form

$$\boldsymbol{y} = \boldsymbol{H}\boldsymbol{x} + \boldsymbol{\epsilon} \tag{18}$$

where $\boldsymbol{y} = \boldsymbol{p} - \boldsymbol{h}\left(\bar{\boldsymbol{x}}, t_k\right) + \boldsymbol{H}\bar{\boldsymbol{x}}$. By virtue of the Gauss–Markov theorem, the best linear unbiased estimate of $\boldsymbol{x}$ is the weighted least-squares solution,[58]

$$\hat{\boldsymbol{x}} = \left(\boldsymbol{H}^T \boldsymbol{R}^{-1} \boldsymbol{H}\right)^{-1} \boldsymbol{H}^T \boldsymbol{R}^{-1} \boldsymbol{y} \tag{19}$$

where $\boldsymbol{R}$ is the pressure measurement error covariance matrix. Since the original relationship between the states and the measurement in Eq. (15) is nonlinear, the estimation scheme can be iterated until convergence by successively replacing $\bar{\boldsymbol{x}}$ by $\hat{\boldsymbol{x}}$, using the converged state estimate from the previous sampling time (t_{k-1}) as the initial reference state $\bar{\boldsymbol{x}}$. The state estimate error covariance matrix $\hat{\boldsymbol{P}}$ can then be computed from

$$\hat{\boldsymbol{P}} = \left(\boldsymbol{H}^T \boldsymbol{R}^{-1} \boldsymbol{H}\right)^{-1} \tag{20}$$

The algorithm can also be iterated globally in order to estimate and remove systematic errors that result from the combination of transducer and CFD distribution uncertainties. After each pass through the pressure data, the residuals are computed as $\boldsymbol{r} = \boldsymbol{p} - \hat{\boldsymbol{p}}$ where $\boldsymbol{p}$ are the measured pressures and $\hat{\boldsymbol{p}}$ are the modeled pressures based on the converged state. The time history of the residuals for each port are then fitted with a second-order polynomial of the form

$$r_i = a_i + b_i p_i + c_i p_i^2 \tag{21}$$

where r_i is the residual for the ith pressure port. The coefficients of the polynomial are determined using a least-squares fit to the residual time history, and are then used to correct the measurements for the next global iteration.

The least–squares solution described in this section has several important properties. First, all pressure measurements are processed simultaneously to determine the atmospheric state variable estimate, opposed to the so-called "triples" algorithms, which use only a subset of available ports to determine the state variable estimates individually in sequence. Using all measurements simultaneously is advantageous in the sense that every port contributes to the state estimate rather than a restricted set, which generally leads to better performance,[57] and is also fault tolerant in the sense that a failed port can simply be removed from the solution that would otherwise ruin a triples algorithm.

The aerodynamic state vector formulation is not unique. In particular, any two variables from the set of p_s, p_t, q, R, and M can be used in the estimator in addition to α and β. The remaining state variables not used directly in the estimator can be calculated as parameters, having first estimated the aerodynamic state variables. Note that the SEADS algorithm[13] made use of p_s and p_t in the estimator formulation.

The quantity R listed above is the pressure ratio. The pressure ratio is a function of the Mach number, which takes the form[13]

$$R = \frac{p_s}{p_t} = \begin{cases} \left[\frac{2}{(\gamma+1)M^2}\right]^{\gamma/(\gamma-1)} \cdot \left[\frac{2\gamma M^2-(\gamma-1)}{\gamma+1}\right]^{1/(\gamma-1)} & \text{for } M > 1 \\[2em] \left[1 + \frac{\gamma-1}{2}M^2\right]^{-\gamma/(\gamma-1)} & \text{for } M \leq 1 \end{cases} \tag{22}$$

The pressure ratio is shown as a function of Mach number for $\gamma = 1.335$ in Fig. 8(a).

The pressure measurement weighting as needed for the MEADS-based pressure reconstruction consists of system error models of transducer characterizations from thermal vacuum chamber calibrations, thermocouple measurement errors such that an inaccurate temperature is used in the calibration database, system noise and quantization, time tag errors and sampling delays, pressure path leaks, pneumatic lag, and thermal transpiration. Additionally, the MEADS weighting includes a model of the CFD uncertainties, which consists of deformation, ablation, outer mold line changes, grid refinement, protuberances, and port location uncertainty. These error models are summarized in Refs. 60–62.

3. Atmosphere Reconstruction

Other atmospheric relative parameters can be estimated from the MEADS pressure solution in conjunction with the IMU measurements and velocity estimates, including the atmospheric density and the basic vehicle force and moment aerodynamic coefficients. First, The freestream atmospheric density follows from the determination of the dynamic pressure from

$$\rho = \frac{2q}{V^2} \tag{23}$$

where V is the IMU-based planet-relative velocity magnitude. The uncertainty in the density estimate can be computed as

$$\sigma_\rho = \left[\left(\frac{\partial \rho}{\partial q}\right)^2 \sigma_q^2 + \left(\frac{\partial \rho}{\partial V}\right)^2 \sigma_V^2\right]^{1/2} = \frac{2}{V^2}\left[\sigma_q^2 + \left(\frac{2q\sigma_V}{V}\right)^2\right]^{1/2} \tag{24}$$

where σ_q is the dynamic pressure uncertainty from the least-squares state covariance matrix, and σ_V is the relative velocity uncertainty computed from linear covariance analysis of the IMU-based reconstruction.

Once computed, the density profile can be integrated using the hydrostatic equation method shown in Eq. (8) to produce another estimate of the freestream static pressure. Then, the density and static pressure estimates can be used to compute an estimate of atmospheric temperature from the equation of state.

It is possible to estimate winds by having both a wind-relative estimate of the aerodynamic flow angles from the pressure-based solution and a planet-relative estimate from the inertial reconstruction, using an approach based on Reference 59. In this approach, the wind components are determined by solving a nonlinear system of algebraic equations that arise by equating the winds to a function of the difference between the wind-relative and planet-relative aerodynamic angles. This method was implemented and tested for application to MSL in Reference 60, but a drawback of the method is that it is singular for zero flight path angle, which presents a serious limitation for application to MSL. Therefore, the method is not proposed for use in MSL EDL data reduction.

4. Aerodynamic Reconstruction

Aerodynamic force and moment coefficients can be estimated by combining the atmospheric state estimates with the sensed accelerations and angular rates from the IMU. The force coefficients can be computed from the equations

$$C_A = -\frac{ma_x}{Sq} \tag{25}$$

$$C_Y = \frac{ma_y}{Sq} \tag{26}$$

$$C_N = -\frac{ma_z}{Sq} \tag{27}$$

where C_A, C_Y, and C_N are the axial, side, and normal force coefficients, respectively. Here, a_x, a_y, and a_z are the body axis sensed accelerations at the vehicle center of mass, m is the vehicle mass, and S is the aerodynamic reference area.

Since the mass, acceleration, and dynamic pressure uncertainties are uncorrelated, simple expressions can be obtained for the uncertainty in the derived axial, normal, and side aerodynamic force coefficients. The expression for the axial force coefficient uncertainty is given in the following equation.

$$\sigma_{C_A} = \left[\left(\frac{\partial C_A}{\partial m} \right)^2 \sigma_m^2 + \left(\frac{\partial C_A}{\partial a_x} \right)^2 \sigma_{a_x}^2 + \left(\frac{\partial C_A}{\partial q} \right)^2 \sigma_q^2 \right]^{1/2} \tag{28}$$

$$= \frac{1}{Sq} \left[a_x^2 \sigma_m^2 + m^2 \sigma_{a_x}^2 + \left(\frac{ma_x}{Sq} \right)^2 \sigma_q^2 \right]^{1/2} \tag{29}$$

Similar expressions can be obtained for the side and normal force coefficients by substituting the appropriate acceleration axis subscript.

A similar approach can be used to determine moment coefficients by making use of angular velocity measurements from the IMU and the estimated spacecraft inertia.

5. Inertial Measurement Unit Aided Estimation Algorithm

As noted in Ref. 13–14, for small pressure ratios (or, equivalently, high Mach) the product RM^2 is nearly constant. This trend is illustrated in Fig. 8(b) for $\gamma = 1.335$. The implications of this trend are twofold. First, any slight change in static pressure has a large impact on the Mach number, which implies that the Mach number is difficult to estimate for low pressure ratios. Secondly, it implies that the dynamic pressure can be computed accurately directly from the total pressure by substituting the limiting value of the quantity RM^2. Therefore, errors in static pressure or Mach number do not contribute to errors in dynamic pressure estimates in the high hypersonic regime.

Due to the asymptotic behavior of the pressure ratio as a function of Mach number, some numerical difficulties in the FADS estimation algorithm can arise for high Mach number conditions. For high Mach cases it can be advantageous to consider a special case of estimators that use a fixed pressure ratio and form state estimates using only three aerodynamic variables, e.g. p_t, α, and β, with dynamic pressure computed directly from p_t assuming the limiting value of the quantity RM^2.[63] These estimators are generally more consistent but become biased as the true pressure ratio drifts away from the assumed value. If the vehicle is instrumented with an IMU then it is also possible to schedule the assumed pressure ratio as a function of the inertial Mach number to reduce the growth of the bias over time. Alternately, the bias can be calibrated and subtracted out using preflight simulation cases.

For application to MSL, a new approach is taken in which the IMU-derived Mach number is used as a pseudo-observation in the least-squares algorithm. In this approach, another equation is added to the observation vector, leading to a system of equations given by

$$\boldsymbol{z} = \tilde{\boldsymbol{h}}\left(\boldsymbol{x}, t_k\right) + \boldsymbol{\epsilon} \tag{30}$$

where

$$\boldsymbol{z} = \left\{ \begin{array}{c} \boldsymbol{p} \\ M \end{array} \right\} \tag{31}$$

American Institute of Aeronautics and Astronautics

(a) Pressure Ratio R

(b) Quantity RM^2
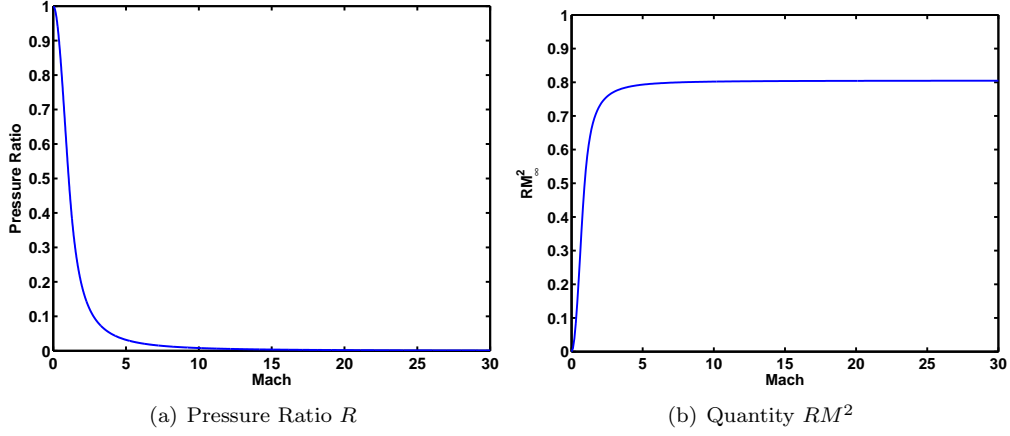
Figure 8: Pressure Ratio vs. Mach for $\gamma = 1.335$

(a) $\partial M/\partial q$

(b) $\partial M/\partial p_s$
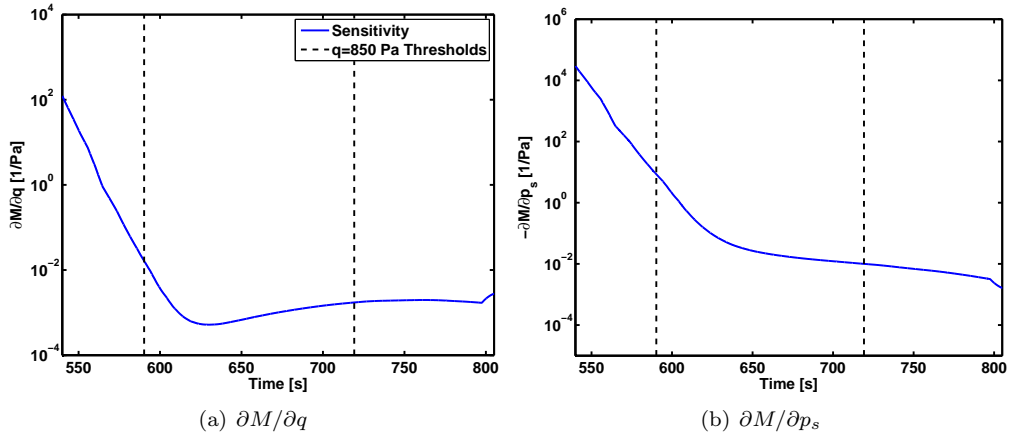
Figure 9: Mach Number Measurement Sensitivities

$$\tilde{\boldsymbol{h}}\left(\boldsymbol{x}, t_k\right) = \left\{ \begin{array}{c} \boldsymbol{h}\left(\boldsymbol{x}, t_k\right) \\ \sqrt{2q/\left(\gamma p_s\right)} \end{array} \right\} \tag{32}$$

Following Sec. III.C.2, the weighted least-squares solution is given by

$$\hat{\boldsymbol{x}} = \left(\tilde{\boldsymbol{H}}^T \tilde{\boldsymbol{R}}^{-1} \tilde{\boldsymbol{H}}\right)^{-1} \tilde{\boldsymbol{H}}^T \tilde{\boldsymbol{R}}^{-1} \tilde{\boldsymbol{y}} \tag{33}$$

where $\tilde{\boldsymbol{y}} = \boldsymbol{z} - \tilde{\boldsymbol{h}}\left(\bar{\boldsymbol{x}}, t_k\right) + \tilde{\boldsymbol{H}}\bar{\boldsymbol{x}}$, $\tilde{\boldsymbol{H}} = [\partial\tilde{\boldsymbol{h}}/\partial\boldsymbol{x}]_{\boldsymbol{x}=\bar{\boldsymbol{x}}}$, and $\tilde{\boldsymbol{R}}$ is the measurement covariance matrix that is augmented with an uncertainty estimate for the Mach number pseudo-observation. The additional components of the measurement sensitivity matrix for the IMU-aiding algorithm are shown in Fig. 9.

Eq. (33) is iterated at each observation time until the state estimate converges (or a maximum number of iterations has been reached). The covariance matrix for the state estimate is given by

$$\hat{\boldsymbol{P}} = \left(\tilde{\boldsymbol{H}}^T \tilde{\boldsymbol{R}}^{-1} \tilde{\boldsymbol{H}}\right)^{-1} \tag{34}$$

To apply the IMU aiding to the least-squares FADS algorithm, an estimate of the speed of sound is needed to compute Mach number from the IMU-derived velocity. This speed of sound estimate can be based on the best available prior atmosphere knowledge. Since the FADS algorithm computes a speed of sound estimate based on the computed density and static pressure, the algorithm can be iterated globally by updating the speed of sound estimate on each pass, based on the derived speed of sound from the previous iteration. Systematic errors are also estimated on each global iteration of the algorithm as described in Sec. III.C.2.

IV. Mars Science Laboratory Entry, Descent, and Landing Data Analysis

A. Data Quality and Preprocessing

The following sections provide details of the various EDL sensor data that were acquired for trajectory and atmosphere reconstruction. These data consist of IMU and pressure sensor data. Also, atmospheric models required for the pure inertial trajectory reconstruction are described.

1. Inertial Measurement Unit Data

Data from the onboard IMU, consisting of ΔVs and $\Delta\theta$s were acquired at a rate of 200 Hz. These velocity and attitude increments were converted into acceleration and angular rate by dividing by the time step for each measurement. A Tustin bilinear filter was used to smooth the data for use in the aerodatabase and MEADS aerodynamic reconstructions. Unfiltered data was integrated for the pure-IMU reconstruction. The filtered and unfiltered IMU data are shown in Fig. 10 for the period from entry interface (540 seconds) to touchdown. Note that considerable noise due to structural vibrations occur during the bank reversal maneuvers where the RCS jets are active. The initial conditions for the integration are based on the orbit determination (OD) number 229, which provides the position and velocity of the vehicle in the Earth Mean Equator of J2000 (EMEJ2000) coordinate system at a time of approximately 550 seconds prior to entry interface.[66,67] The attitude initialization was based on the on-board navigation filter that performed a star tracker alignment prior to cruise stage separation. This attitude solution was then propagated to the same initial time as the OD229 solution by numerical integration.

2. Pressure Data

The MEADS pressure measurement data were acquired at an 8 Hz sample rate during EDL. For EDL reconstruction, the data were first converted into engineering units, after which an in-flight zero was applied to correct for transducer thermal drift. Subsequently, outlying data points due to the entry ballast mass ejections were edited out and filled in with a first-order polynomial fit, and a 1 Hz optimal Fourier filter was applied to smooth the data. The pressures were then interpolated to the Port 4 time tag in order to generate pressure samples at a common 8 Hz rate. The resulting pressures are compared to pre-flight nominal trajectory predictions based on OD 213 in Figs. 11–13. Fig. 11 shows comparisons for the stagnation region, Ports 1 and 2. Fig. 12 shows the comparisons for the ports along the spherical cap, Ports 3–5, and Fig. 13 shows comparisons for Ports 6 and 7, which provide the primary measurement of the sideslip angle. These figures illustrate that the sensor readings during EDL are reasonable, and that all transducers are functional. Data quality during EDL was good for the majority of the trajectory. Some noise was introduced during pyro events associated with mass ejections during the reorientation to zero angle of attack in preparation for parachute deployment. Vibrations induced by the parachute mortar fire event were large, which further reduced the MEADS data quality. This vibrational noise, coupled with the rapid decrease in dynamic pressure following parachute deployment, essentially limited the last valid MEADS measurement to the instant prior to parachute mortar fire. Other aspects of MEDLI hardware performance during EDL are described in Ref. 64.

3. Atmospheric Models

Atmospheric models along the MSL EDL trajectory were generated from preflight mesoscale models, described in Ref. 65, tuned to match surface pressure measurements of 695 Pa from Curiosity, which were obtained after landing. The modeled atmosphere is an average of two such mesoscale models, namely the Mars Mesoscale Model 5 (MMM5) and the Mars Regional Atmospheric Modeling System (MRAMS). These models provide data up to 50 km altitude, which can be extrapolated to higher altitudes as needed. This combined model was queried along the IMU-navigated trajectory at time increments of 0.5 seconds to generate pressure, density, and temperature profiles. These profiles were then interpolated by altitude in order to provide atmospheric-relative estimates (Mach number and dynamic pressure) for the pure IMU reconstruction.
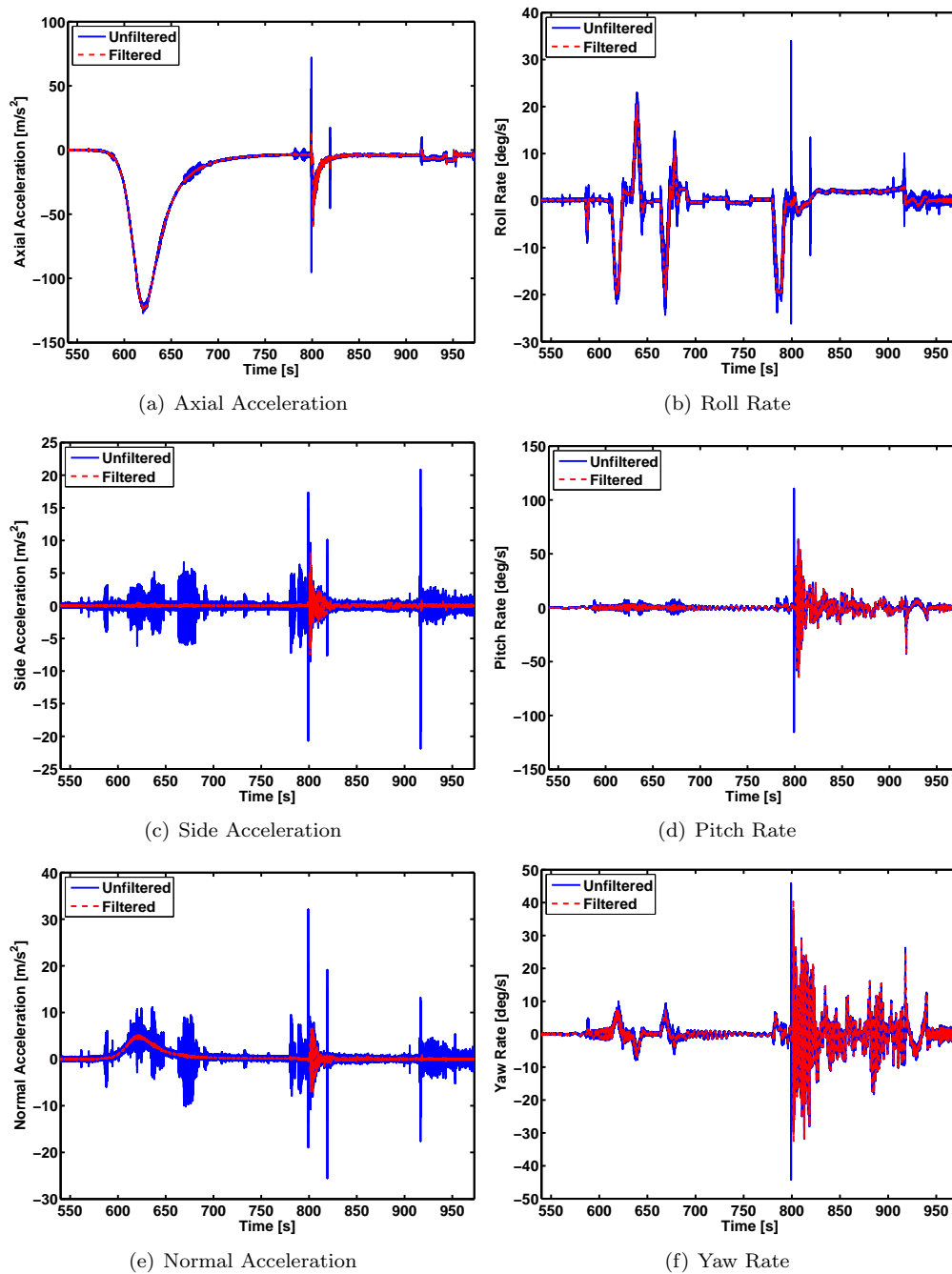
American Institute of Aeronautics and Astronautics

(a) Axial Acceleration

(b) Roll Rate

(c) Side Acceleration

(d) Pitch Rate

(e) Normal Acceleration

(f) Yaw Rate

Figure 10: Sensed Accelerations and Angular Rates

B. Reconstruction Results

Results of the three independent reconstructions are described in the following subsections. These sections describe the reconstructions of the aerodynamic state, free stream atmosphere, and vehicle aerodynamics.

1. Aerodynamic State Reconstruction

The aerodynamic state reconstructions are shown in Fig. 14. Fig. 14(a) shows results for the angle of attack, Fig. 14(b) shows results for the angle of sideslip, Fig. 14(c) shows results for dynamic pressure, and Fig. 14(d) shows results for the Mach number estimate. In each of these plots, the pure-IMU reconstruction is shown in
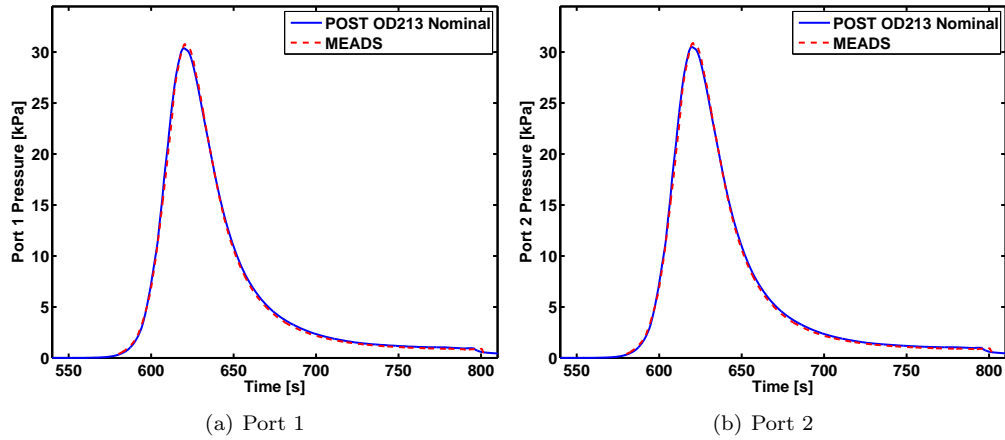
American Institute of Aeronautics and Astronautics

(a) Port 1

(b) Port 2

Figure 11: MEADS Port 1 and 2 Pressures
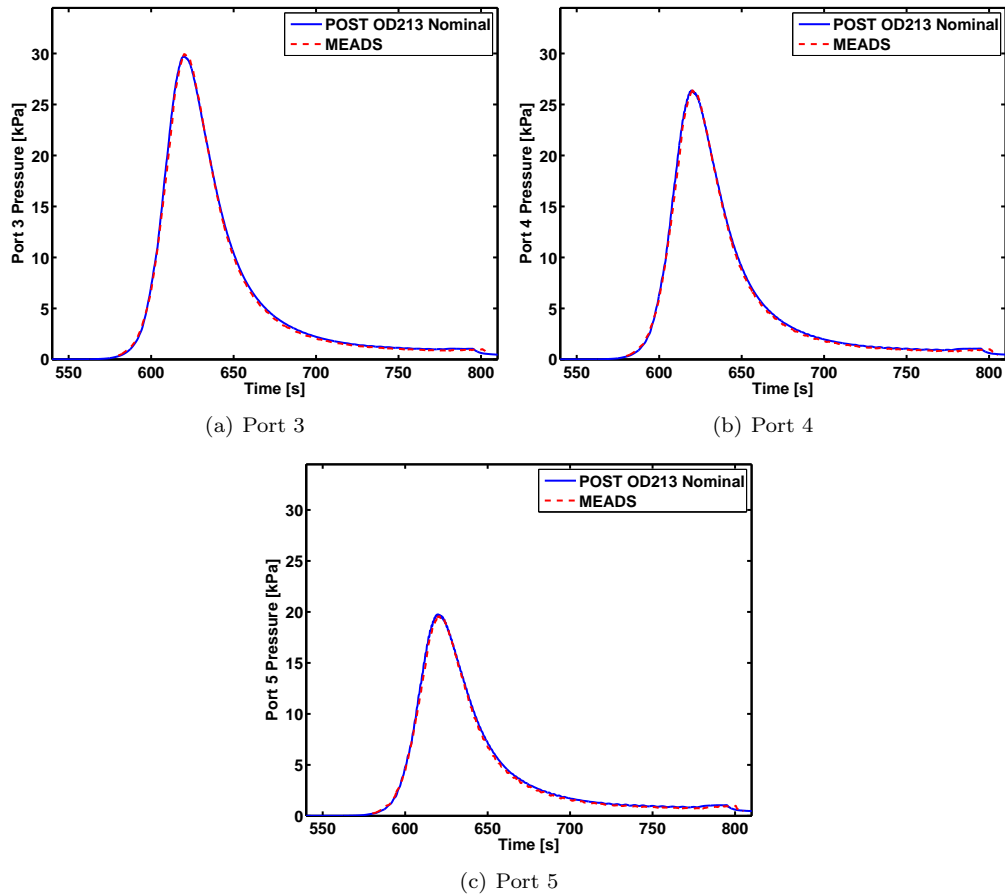

(a) Port 3

(b) Port 4

(c) Port 5

Figure 12: MEADS Port 3-5 Pressures

blue, the aerodatabase reconstruction is shown in red, and the IMU-aided MEADS pressure reconstruction is shown in cyan. The three reconstructions give fairly consistent results. The hypersonic trim angle predicted by the pure-IMU reconstruction closely matches the predicted trim angle based on the aerodatabase, which is shown in the black curve in Fig. 14(a). There are differences in angle of attack on the order of 0.4 degrees between the inertial, MEADS, and ADB reconstructions in the hypersonic regime. The three reconstructions
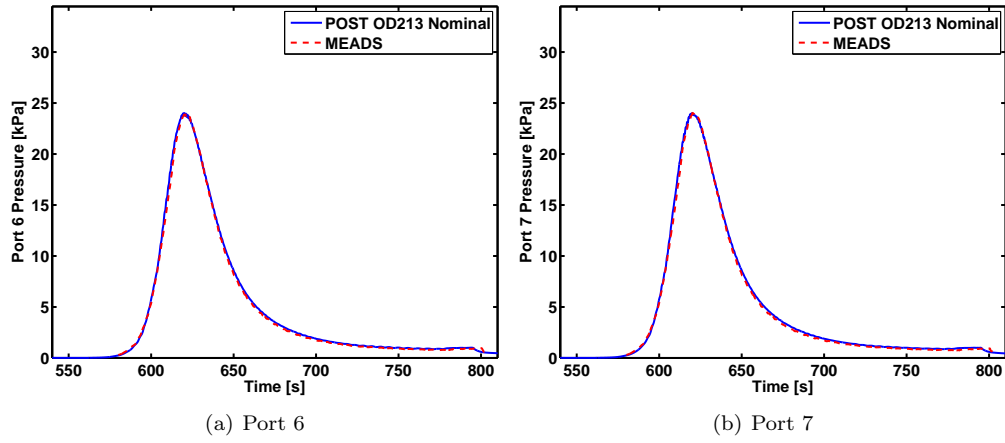
American Institute of Aeronautics and Astronautics

(a) Port 6

(b) Port 7

Figure 13: MEADS Port 6 and 7 Pressures

(a) Angle of Attack

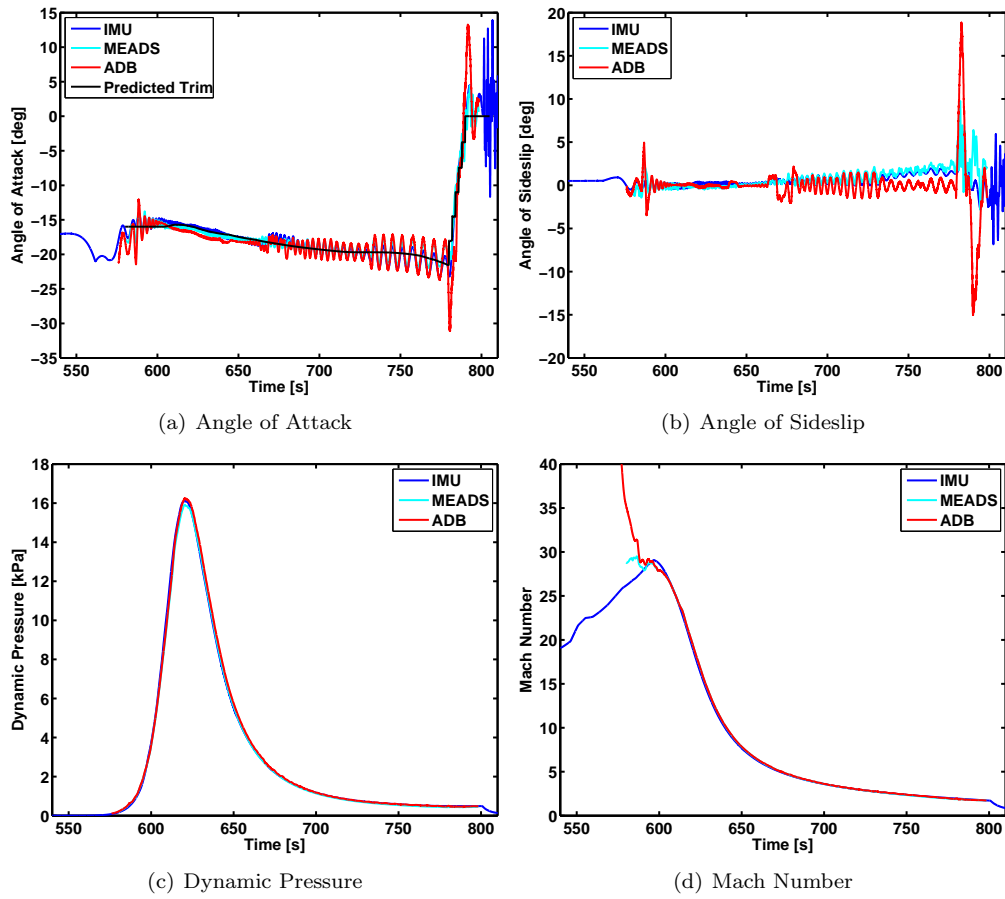(b) Angle of Sideslip

(c) Dynamic Pressure

(d) Mach Number

Figure 14: Aerodynamic State Reconstruction

are in better agreement in the supersonic regime.

2. Atmospheric Reconstruction

The atmospheric reconstructions are shown in Fig. 15. Fig. 15(a–b) show results for the estimate of density, Fig. 15(c–d) show results of the static pressure estimate, and Fig. 15(e–f) show the results of the temperature

(a) Density vs. Time

(b) Density vs. Altitude

(c) Pressure vs. Time

(d) Pressure vs. Altitude

(e) Temperature vs. Time
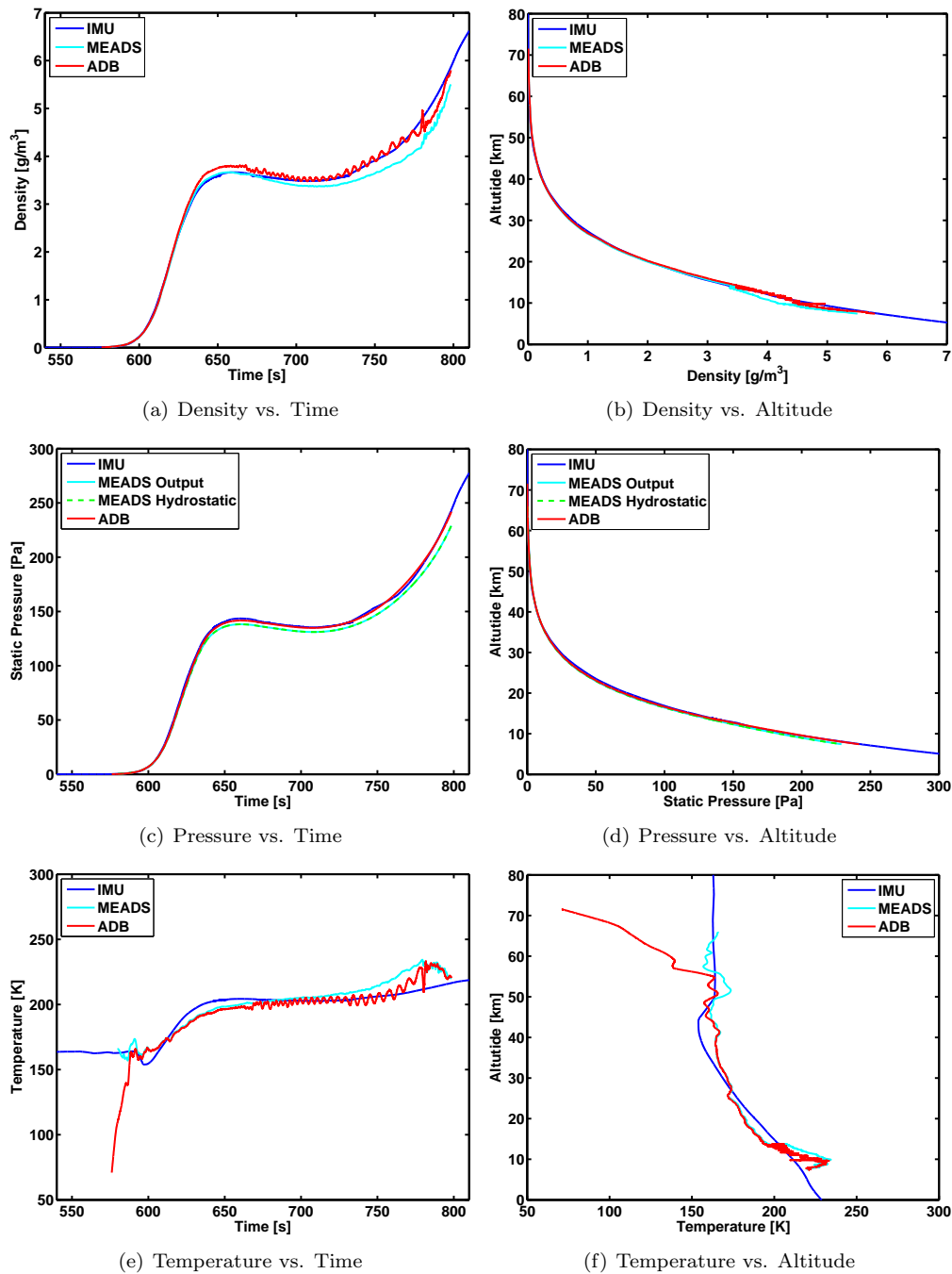
(f) Temperature vs. Altitude

Figure 15: Atmosphere Reconstruction

reconstruction. In each case, the left plot shows the results as functions of time along the trajectory whereas the right plot shows the results as a function of altitude. Note that the IMU reconstruction here refers to the mesoscale model queried along the reconstructed altitude profile. Two MEADS reconstructions of static pressure are shown in Fig. 15(c–d). Here, the cyan curve shows the static pressure estimate that is produced directly from the least-squares processing algorithm, whereas the dashed green curve shows the static pressure estimate that is produced from a hydrostatic integration of the derived density profile. These two reconstructions are in close agreement, with maximum differences on the order of 0.02%. The initial condition for the hydrostatic integration was obtained from the combined mesoscale atmosphere model at an altitude of 66 km. The three reconstructions are in fairly good agreement until an altitude of 13-14 km.

American Institute of Aeronautics and Astronautics

Recall that the MEADS derived density assumes that the atmospheric winds are zero relative to the rotation of the planet. As the vehicle decelerates, any non-zero wind becomes larger in proportion to the IMU-based planet relative velocity, and these winds produce an error in the density estimate. A question that naturally arises is when and at what altitude do these potential errors become important to the reconstruction. To answer this question, a simple wind sensitivity study was conducted in which a 20 m/s tail or head wind (represented by a pure east/west wind component) was included in the estimated relative velocity based on the IMU integration. The results are shown in Fig. 16(a) and (b), where the results are shown as functions of time and altitude, respectively. The results of the nominal zero wind case are also shown for comparison. The differences between the reconstructions starts to become apparent at a time of roughly 640-650 seconds, corresponding to an altitude of 13-14 km. Interestingly, this is the same altitude range where the nominal MEADS reconstruction begins to differ from the mesoscale model. These results suggests that the differences between the MEADS reconstruction and the mesoscale model could be reconciled with a reasonable tail wind.
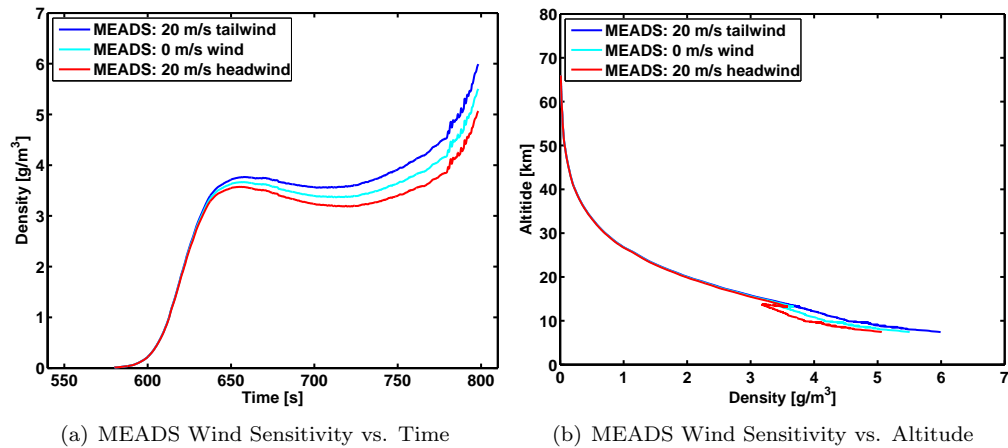

(a) MEADS Wind Sensitivity vs. Time   (b) MEADS Wind Sensitivity vs. Altitude

Figure 16: MEADS Wind Sensitivity

3. *Aerodynamic Reconstruction*

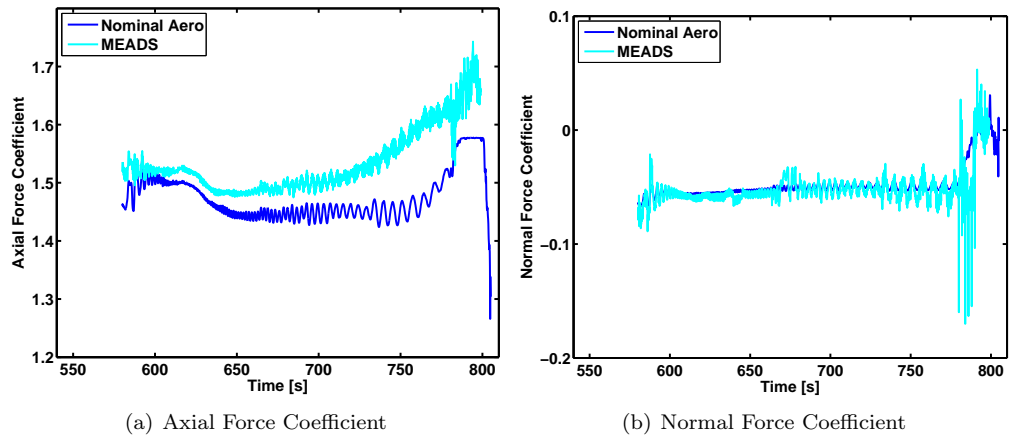(a) Axial Force Coefficient   (b) Normal Force Coefficient

Figure 17: Aerodynamic Reconstruction

The MEADS-based reconstruction of the vehicle aerodynamics is shown in this section. Fig. 17(a) shows the axial force reconstruction and Fig. 17(b) shows the normal force reconstruction. In each case, the MEADS-based reconstruction is shown in the cyan curve, and the nominal aerodatabase queried at the MEADS-derived atmospheric flight condition is shown in the blue curve. The MEADS results indicate

American Institute of Aeronautics and Astronautics

a slightly higher drag than the nominal prediction. Complete analysis and model reconciliation of the aerodynamic reconstruction is beyond the scope of this paper. More detailed analysis of the MSL entry vehicle aerodynamic performance are provided in Ref. 68.

4. MEADS Pressure Residuals

(a) Port 1: Pascals

(b) Port 1: Percent

(c) Port 2: Pascals
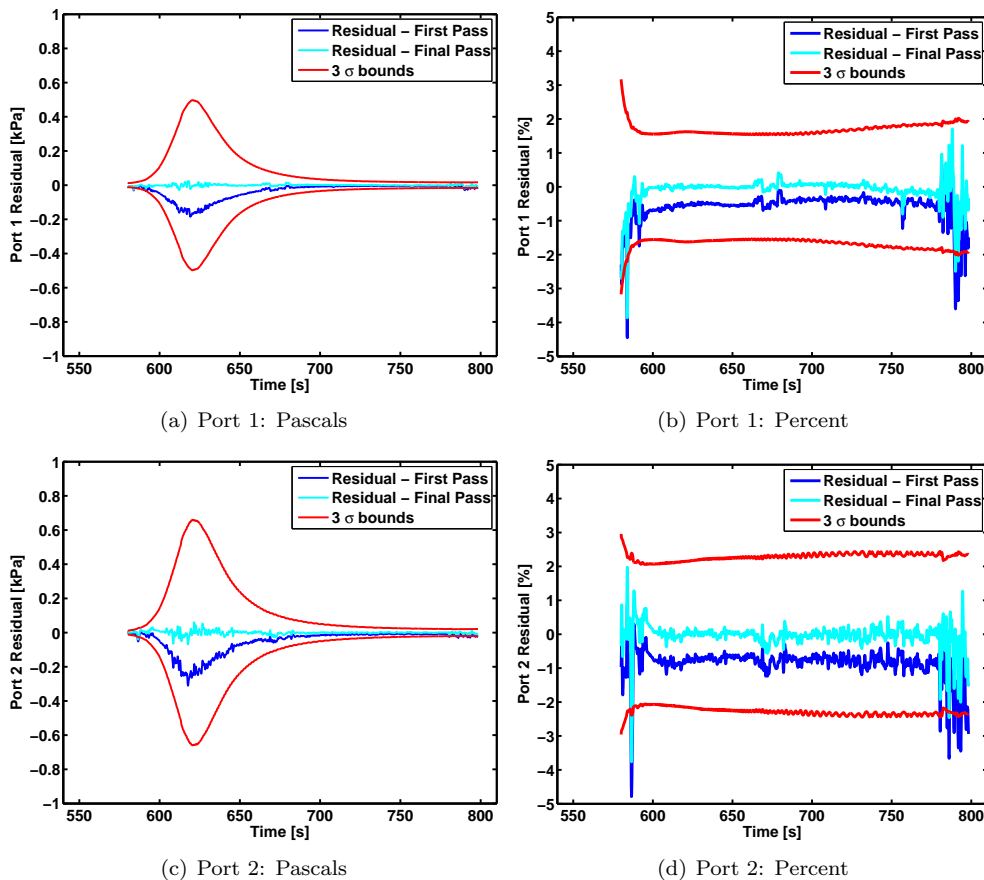
(d) Port 2: Percent

Figure 18: Port 1 and 2 Residuals

This section shows the pressure residuals from the IMU-aided MEADS reconstruction. Recall that the first pass of the algorithm assumes an isothermal atmosphere with no systematic errors, and subsequent passes iterate to solve for the atmospheric conditions and to determine systematic errors. The pressure residuals are expected to reduce as a consequence of these iterations. The results based on the MEADS flight data are shown in Figs. 18–20. These plots show the residuals for Ports 1–2, 3–5, and 6–7, respectively. In each case, the residual based on the first iteration is shown in the blue curve and the residual based on the final converged solution is shown in cyan. Also, the 3σ uncertainty bands that include measurement system uncertainties as well as CFD pressure model uncertainties are shown. The left column of figures shows the residual in units of pressure whereas the right column shows the residuals as percent of reading. These plots indicate that the IMU-aided MEADS algorithm is successfully able to reduce the residuals and remove systematic error by iterating on the atmosphere and systematic error parameters. The resulting residuals are well within the expected 3σ uncertainty bands and roughly zero mean, which is another indication of good transducer performance during EDL. The Root Mean Square (RMS) residuals and estimates of systematic error parameters over the period of good quality data (roughly 590-775 seconds) are summarized in Table 1.
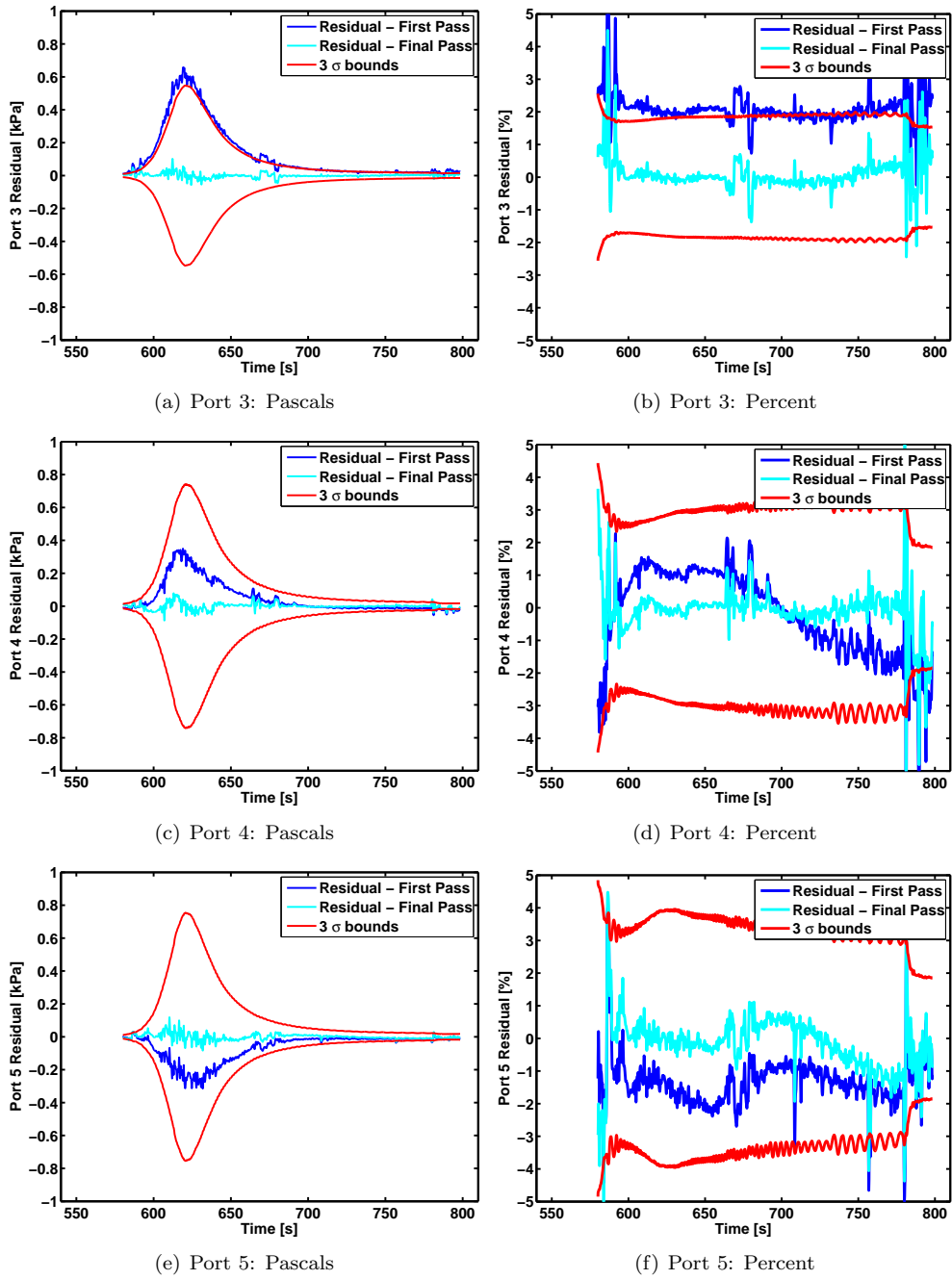
American Institute of Aeronautics and Astronautics

(a) Port 3: Pascals

(b) Port 3: Percent

(c) Port 4: Pascals

(d) Port 4: Percent

(e) Port 5: Pascals

(f) Port 5: Percent

Figure 19: Port 3-5 Residuals

American Institute of Aeronautics and Astronautics

(a) Port 6: Pascals   (b) Port 6: Percent

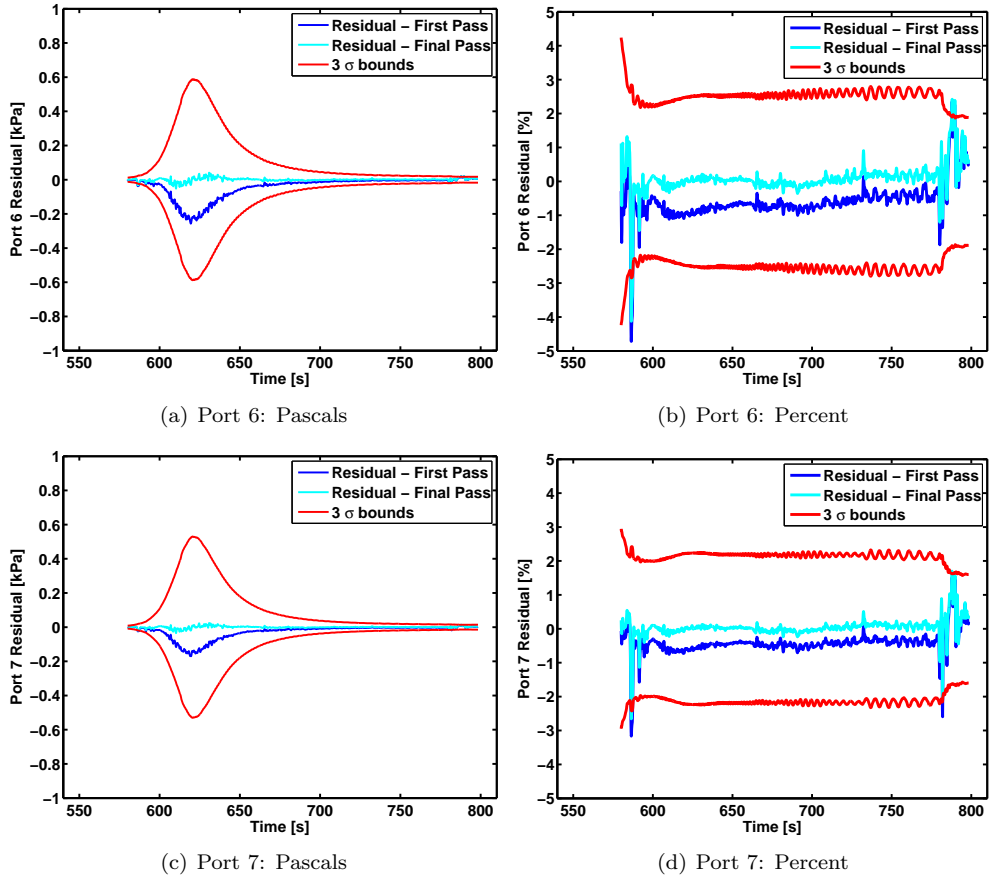(c) Port 7: Pascals   (d) Port 7: Percent

Figure 20: Port 6 and 7 Residuals

Table 1: RMS Pressure Residuals and Systematic Error Estimates

Port	Residual RMS Error		Systematic Error Estimates		
	First Iteration (Pa)	Final Iteration (Pa)	Bias (Pa)	Scale Factor	Nonlinearity (1/Pa)
1	62.76	5.14	1.75	-6.28E-03	3.72E-08
2	91.31	11.30	-1.67	-6.80E-03	-3.23E-08
3	234.55	14.35	-1.77	2.23E-02	-9.10E-08
4	115.16	18.70	-25.51	1.57E-02	-1.59E-07
5	110.73	19.41	11.67	-2.41E-02	5.65E-07
6	80.68	9.50	0.56	-6.05E-03	-1.41E-07
7	52.09	6.07	-0.99	-3.50E-03	-1.08E-07

American Institute of Aeronautics and Astronautics

V.   Conclusions

This paper describes three complimentary reconstruction methods that have been implemented for Mars Science Laboratory entry, descent, and landing trajectory reconstruction. Each of these methods makes use of a different subset of the total available data to reconstruct portions of the trajectory. Specifically, the methods include a pure inertial reconstruction, a reconstruction based on the nominal aerodatabase, and a reconstruction based on measurements of the forebody surface pressure distribution. The first two of these methods are considered standard approaches for Mars entry, descent, and landing reconstruction, whereas the latter of these techniques is new to this application. The pressure-based reconstruction is enabled by instrumentation consisting of transducer measurements from seven pressure ports on the vehicle heatshield. Such heatshield pressure data has not successfully been collected during Mars entry prior to Mars Science Laboratory. A novel inertial measurement unit-aided estimation approach is introduced in this paper for processing these pressure measurements, wherein the planet-relative velocity is utilized to help anchor the pressure-derived Mach number estimates, which otherwise are nearly unobservable with pressures alone. An important feature of the new pressure-based reconstruction technique is that it allows for an atmosphere reconstruction to be conducted without assumptions on the vehicle aerodynamics. This in turn allows for an aerodynamic reconstruction to be performed, which has not been possible for Mars entry reconstructions of the past.

These algorithms are utilized to process flight data from Mars Science Laboratory's atmospheric entry at Mars, which occurred on August 5th 2012. Assessments of the pressure measurements indicate that the data quality is good. Vibrations from pyrotechnic events effectively limit the last valid pressure measurement to the instant prior to parachute mortar fire. The three reconstruction methods are generally in good agreement. The pure inertial reconstruction of angle of attack is in close agreement to the preflight predicted trim angle. The reconstructed atmosphere profile from the pressure reconstruction is in reasonable agreement with atmospheric models that were tuned to match surface pressure measurements from the Curiosity rover until an altitude of approximately 13-14 km. In this altitude range the pressure-based reconstruction becomes sensitive to atmospheric winds, which could account for the drift away from the modeled atmosphere profile. The overall good data quality and general agreement between the reconstructions supports a future combined reconstruction involving Kalman filtering techniques to optimally blend all available data together into a single trajectory and atmosphere estimate.

Acknowledgements

References

[1]Grotzinger, J. P., Crisp, J., Vasavada, A. R., Anderson, R. C., Baker, C. J., Barry, R., Blake, D. F., Conrad, P., Edgett, K. S., Ferdowski, B., Gellert, R., Gilbert, J. B., Golombek, M., Gomez-Elvira, J., Hassler, D. M., Jandura, L., Litvak, M., Mahaffy, P., Maki, J., Meyer, M., Malin, M. C., Mitrofanov, I., Simmonds, J. J., Vaniman, D., Welch, R. V., and Wiens, R. C., "Mars Science Laboratory Mission and Science Investigation," *Space Science Reviews*, Vol. 170, 2012, pp. 5–56.

[2]Gazarik, M. J., Wright, M. J., Little, A., Cheatwood, F. M., Herath, J. A., Munk, M. M., Novak, F. J., and Martinez, E. R., "Overview of the MEDLI Project," IEEE 2008 Aerospace Conference, March 2008.

[3]Larson, T. J. and Webb, L. D., "Calibrations and Comparisons of Pressure–Type Airspeed–Altitude Systems of the X-15 Airplane from Subsonic to High Supersonic Speeds," NASA TN D–1724, February 1963.

[4]Cary, J. P. and Keener, E. R., "Flight Evaluation of the X-15 Ball–Nose Flow–Direction Sensor as an Air–Data System," NASA TN D–2923, July 1965.

[5]Ingoldby, R., Michel, F., Flaherty, R., Doty, M., Preston, B., Villyard, K., and Steele, R., "Entry Data Analysis for Viking Landers 1 and 2," NASA CR-159388, 1976.

[6]Wolf, H. and Eades, J. B., "Analysis of the Shuttle Air Data System," NASA CR-145279, October 1977.

[7]Siemers, P. M. and Larson, T. J., "Space Shuttle Orbiter and Aerodynamic Testing," *Journal of Spacecraft and Rockets*, Vol. 16, No. 4, 1979, pp. 223–231.

[8]Larson, T. J., Flechner, S. G., and Siemers, P. M., "Wind Tunnel Investigation of an All Flush Orifice Air Data System for a Large Subsonic Aircraft," NASA TP–1642, May 1980.

[9]Larson, T. J. and Siemers, P. M., "Use of Nose Cap and Fuselage Pressure Orifices for Determination of Air Data for Space Shuttle Orbiter Below Supersonic Speeds," NASA TP-1643, September 1980.

[10]Larson, T. J. and Siemers, P. M., "Subsonic Tests of an All-Flush-Pressure-Orifice Air Data System," NASA TP-1871, June 1981.

[11]Bradley, P. F., Siemers, P. M., and Weilmuenster, K. J., "Comparison of Shuttle Flight and Pressure Data to Computational and Wind-Tunnel Results," *Journal of Spacecraft and Rockets*, Vol. 19, No. 5, 1982, pp. 419–422.

[12]Bradley, P. F., Siemers, P. M., and Weilmuenster, K. J., "Comparison of Shuttle Orbiter Surface Pressures with Wind Tunnel and Theoretical Predictions," *Journal of Spacecraft and Rockets*, Vol. 21, No. 3, pp. 227–233.

[13]Pruett, C. D., Wolf, H., Heck, M. L., and Siemers, P. M., "Innovative Air Data System for the Space Shuttle Orbiter," *Journal of Spacecraft and Rockets*, Vol. 20, No. 1, 1983, pp. 61–69.

[14]Siemers, P. M., Wolf, H., and Flanagan, P. F., "Shuttle Entry Air Data System Concepts Applied to Space Shuttle Orbiter Flight Pressure Data to Determine Air Data – STS 1-4," AIAA Paper 83–018, January 1983.

[15]Siemers, P. M., Bradley, P. F., Wolf, H., Flanagan, P. F., Weilmuenster, K. J., and Kern, F. A., "Shuttle Flight Pressure Instrumentation: Experience and Lessons for the Future," NASA Langley Conference on Shuttle Performance: Lessons Learned, Hampton, VA, March 1983.

[16]Wolf, H., Flanagan, P. F., and Henry, H. W., "Shuttle Entry Air Data System Program Manual," Analytical Mechanics Associates, Inc., AMA Report 85–4, March 1985.

[17]Henry, M. W., Wolf, H., and Siemers, P. M., "An Evaluation of Shuttle Entry Air Data (SEADS) Flight Pressures: Comparisons with Wind Tunnel and Theoretical Predictions," AIAA Paper 88-2052, May 1988.

[18]Wolf, H., Henry, M. W., and Siemers, P. M., "Shuttle Entry Air Data System (SEADS): Optimization of Preflight Algorithms Based on Flight Results," AIAA Paper 88-2053, May 1988.

[19]Gibson, F. A., Henry, M. W., and Eades, J. B., Jr., "Shuttle Entry Air Data System (SEADS) Data Analysis: A Historical Perspective," Analytical Mechanics Associates, Inc., AMA Report 92–7, December 1992.

[20]Woeste, T. J., "Shuttle Entry Air Data System - An Experimental Investigation of Calibration for Ascent Flight," *Acta Astronautica*, Vol. 28, 1992, pp. 409–417.

[21]Siemers, P. M., Henry, M. W., and Eades, J. B., "Shuttle Entry Air Data System (SEADS) - Advanced Air Data System Results: Air Data Across the Entry Speed Range," *Orbiter Experiments (OEX) Aerothermodynamics Symposium*, NASA CP-3248, Part I, April 1995, pp. 49–78.

[22]Throckmorton, D. A., "Shuttle Entry Aerothermodynamic Flight Research: The Orbiter Experiments Program," *Journal of Spacecraft and Rockets*, Vol. 30, No. 4, 1993, pp. 449–465.

[23]Brown, E. N., Friehe, C. A., and Lenschow, D. H., "The Use of Pressure Fluctuations on the Nose of an Aircraft for Measuring Air Motion," *Journal of Climate and Applied Meteorology*, Vol. 22, No. 1, 1983, pp. 171–180.

[24]Larson, T. J., Whitmore, S. A., Ehernberger, L. J., Johnson, J. B., and Siemers, P. M., "Qualitative Evaluation of a Flush Air Data System at Transonic Speeds and High Angles of Attack," NASA TP-2716, April 1987.

[25]Anderson, M. B., Lawrence, W. R., and Lopez, J. L., "Air Data Prediction from Surface Pressure Measurements on Guided Munitions," *Journal of Guidance, Control, and Dynamics*, Vol. 18, No. 2, 1995, pp. 355–360.

[26]Gibson, L. S., Siemers, P. M., and Kern, F. A., "Pressure Distribution and Air Data System for the Aeroassist Flight Experiment," International Instrumentation Symposium, ISA Paper 89-0048, May 1989.

[27]Gibson, L. S. and Sealey, B. S., "Test and Evaluation of Pressure Transducers for a Reentry Vehicle Pressure Measurement System," International Instrumentation Symposium, ISA Paper 93-0141, May 1993.

[28]Whitmore, S. A. and Moes, T. R., "Measurement Uncertainty and Feasibility Study of a Flush Airdata System for a Hypersonic Flight Experiment," NASA TM 4627, 1994.

[29]Whitmore, S. A., Davis, R. J., and Fife, J. M., "In–Flight Demonstration of a Real–Time Flush Airdata Sensing System," *Journal of Aircraft*, Vol. 33, No. 5, 1996, pp. 970–977.

[30]Takaki, R. and Takizawa, M., "ADS Measurement of HYFLEX (HYpersonic FLight EXperiment)," AIAA Paper 97-0193, January 1997.

[31]Whitmore, S. A., Cobleigh, B. R., and Haering, E. A., "Design and Calibration of the X–33 Flush Airdata Sensing (FADS) System," AIAA Paper 98-0201, January 1998.

[32]Cobleigh, B. R., Whitmore, S. A., Haering, E. A., Borrer, J., and Roback, V. E., "Flush Airdata Sensing (FADS) System Calibration Procedures and Results For Blunt Forebodies," AIAA Paper 99-4816, November 1999.

[33]Davis, M. C., Pahle, J. W., White, J. T., Marshall, L. A., Mashburn, M. J., and Franks, R., "Development of a Flush Airdata Sensing System on a Sharp–Nosed Vehicle for Flight at Mach 3 to 8," AIAA Paper 2000-0504, January 2000.

[34]Baumann, E., Pahle, J. W., Davis, M. C., and White, J. T., "X-43A Flush Airdata Sensing System Flight–Test Results," *Journal of Spacecraft and Rockets*, Vol. 47, No. 1, 2010, pp. 48–61.

[35]Ellsworth, J. C. and Whitmore, S. A., "Simulation of a Flush Air–Data System for Transatmospheric Vehicles," *Journal of Spacecraft and Rockets*, Vol. 45, No. 4, 2008, pp. 716–732.

[36]Ali, A. N. and Borrer, J., "PA-1 Flush Air Data Sensing Systems," Invited Presentation, AIAA Aerospace Sciences Meeting, Orlando, FL, January 2011.

[37]Kowal, T. J., "Orion Flight Test-1 Thermal Protection System Instrumentation," 8th International Planetary Probe Workshop, Portsmouth, VA, June 2011.

[38]Santos, J. A., Oishi, T., and Martinez, E. R., "Isotherm Sensor Calibration Program for Mars Science Laboratory Heat Shield Flight Data Analysis," AIAA Paper 2011-3955, June 2011.

[39]White, T., Cozmuta, I., Santos, J. A., Laub, B., and Mahzari, M., "Proposed Analysis Process for Mars Science Laboratory Heat Shield Sensor Plug Flight Data," AIAA Paper 2011-3957, June 2011.

[40]Mahzari, M., Cozmuta, I., Clark, I. G., and Braun, R. D., "An Inverse Parameter Estimation Methodology for the Analysis of Aeroheating and Thermal Protection System Experimental Data," AIAA Paper 2011-4027, June 2011.

[41]Abilleira, F. and Shidner, J., "Entry, Descent, and Landing Communications for the 2011 Mars Science Laboratory," Paper IN1-4, 23rd International Symposium on Space Flight Dynamics, Pasadena, CA, October 2012.

[42]Steltzner, A. D., Burkhart, P. D., Chen, A., Comeaux, K. A., Guernsey, C. S., Kipp, D. M., Lorenzoni, L. V., Mendeck, G. F., Powell, R. W., Rivellini, T. P., San Martin, A. M., Sell, S. W., Prakash, R., and Way, D. D., "Mars Science Laboratory Entry, Descent, and Landing System Overview," 7th International Planetary Probe Workshop, Barcelona, Spain, June 2010.

[43]Euler, E. A., Adams, G. L., and Hopper, F. W., "Design and Reconstruction of the Viking Lander Descent Trajectories," *Journal of Guidance and Control*, Vol. 1, No. 5, 1978, pp. 372–378.

[44]Spencer, D. A., Blanchard, R. C., Braun, R. D., Kallemeyn, P. H., and Thurman, S. W., "Mars Pathfinder Entry, Descent, and Landing Reconstruction," *Journal of Spacecraft and Rockets*, Vol. 36, No. 3, 1999, pp. 357–366.

[45]Withers, P., Towner, M. C., Hathi, B., and Zarnecki, J. C., "Analysis of Entry Accelerometer Data: A Case Study of Mars Pathfinder," *Planetary and Space Science*, Vol. 51, 2003, pp. 541–561.

[46]Withers, P. and Smith, M. D., "Atmospheric Entry Profiles from the Mars Exploration Rovers Spirit and Opportunity," *Icarus*, Vol. 185, 2006, pp. 133-142.

[47]Blanchard, R. C., "Entry Descent and Landing Trajectory and Atmosphere Reconstruction for the Mars Exploration Rovers Missions A and B," George Washington University, Final Report, NASA-JPL Subcontract CCNS20568F, April 15th, 2008.

[48]Blanchard, R. C. and Desai, P. N., "Mars Phoenix Entry, Descent, and Landing Trajectory and Atmosphere Reconstruction," *Journal of Spacecraft and Rockets*, Vol. 48, No. 5, 2011, pp. 809–821.

[49]Wagner, W. E., "Re-Entry Filtering, Prediction, and Smoothing," *Journal of Spacecraft and Rockets*, Vol. 3, No. 9, 1966, pp. 1321–1327.

[50]Wagner, W. E. and Serold, A. C., "Formulation on Statistical Trajectory Estimation Programs," NASA CR-1482, January 1970.

[51]Karlgaard, C. D., Tartabini, P. V., Blanchard, R. C., Kirsch, M., and Toniolo, M. D., "Hyper–X Post–Flight Trajectory Reconstruction," *Journal of Spacecraft and Rockets*, Vol. 43, No. 1, 2006, pp. 105–115.

[52]Karlgaard, C. D., Tartabini, P. V., Martin, J. G., Blanchard, R. C., Kirsch, M., Toniolo, M. D., and Thornblom, M. N., "Statistical Estimation Methods for Trajectory Reconstruction: Application to Hyper-X," NASA TM-2009-215792, August 2009.

[53]Karlgaard, C. D., Beck, R. E., Derry, S. D., Brandon, J. M., Starr, B. R., Tartabini, P. V., and Olds, A. D., "Ares I-X Trajectory Reconstruction: Methodology and Results," *Journal of Spacecraft and Rockets*, accepted.

[54]Schoenenberger, M., Dyakonov, A., Buning, P., Scallion, W., and Van Norman, J., "Aerodynamic Challenges for the Mars Science Laboratory Entry, Descent and Landing," AIAA Paper 2009-3914, June 2009.

[55]Dyakonov, A., Schoenenberger, M., and Van Norman, J., "Hypersonic and Supersonic Static Aerodynamics of Mars Science Laboratory Entry Vehicle," AIAA Paper 2012-2999, June 2012.

[56]Camac, M., "CO2 Relaxation Process in Shock Waves," in *Fundamental Phenomena in Hypersonic Flow*, Hall, J. G. (Ed.), Cornell University Press, Ithaca, New York, 1966.

[57]Weiss, S., "Comparing Three Algorithms for Modeling Flush Air Data Systems," AIAA Paper 2002–0535, January 2002.

[58]Crassidis, J. L. and Junkins, J. L., *Optimal Estimation of Dynamic Systems*, Chapman & Hall/CRC, Boca Raton, FL, 2004.

[59]Kelly, G. M., Findlay, J. T., and Compton, H. R., "Shuttle Subsonic Horizontal Wind Estimation," *Journal of Spacecraft and Rockets,* Vol. 20, No. 4, 1983, pp. 390–397.

[60]Karlgaard, C. D., Beck, R. E., O'Keefe, S. A., Siemers, P. M., White, B. A., Engelund, W. C., and Munk, M. M., "Mars Entry Atmospheric Data System Modeling and Algorithm Development," AIAA Paper 2009-3916, June 2009.

[61]Karlgaard, C. D. and Siemers, P. M., "SSE-07 and Replacement MEADS Flight Final Calibration Test Report," MEDLI-0238, February 2011.

[62]Munk, M. M., Karlgaard, C. D., and Schoenenberger, M., "MEADS Error Budget Report," MEDLI-0239, August 2011.

[63]Deshpande, S. M., Kumar, R. R., Seywald, H., and Siemers, P. M., "Air Data System Optimization Using a Genetic Algorithm," AIAA Paper 92-4466, 1992.

[64]Little, A., Munk, M., Schoenenberger, M., Kuhl, C., Antill, C., Verhappen, R., Karlgaard, C., Kutty, P., Bose, D., and White, T., "The Mars Science Laboratory (MSL) Entry, Descent and Landing Instrumentation (MEDLI): Hardware Performance and Data Reconstruction," AAS Paper 13-078, AAS Guidance and Control Conference, Breckenridge, CO, February 2013, to appear.

[65]Vasavada, A. R., Chen, A., Barnes, J. R., Burkhart, P. D., Cantor, B. A., Dwyer-Cianciolo, A. M., Fergason, R. L., Hinson, D. P., Justh, H. L., Kass, D. M., Lewis, S. R., Mischna, M. A., Murphy, J. R., Rafkin, S. C. R., Tyler, D., and Withers, P. G., "Assessment of Environments for Mars Science Laboratory Entry, Descent, and Surface Operations," *Space Science Reviews*, Vol. 170, 2012, pp. 793–835.

[66]Martin-Mur, T. J., Kruizinga, G. L., Burkhart, P. D., Wong, M. C., and Abilleira, F., "Mars Science Laboratory Navigation Results," Paper IN1-1, 23rd International Symposium on Space Flight Dynamics, Pasadena, CA, October 2012.

[67]Kruizinga, G. L., Gustafson, E. D., Thompson, P. F., Jefferson, D. C., Martin-Mur, T. J., Mottinger, N. A., Pelletier, F. J., and Ryne, M. S., "Mars Science Laboratory Orbit Determination Results," Paper IN1-3, 23rd International Symposium on Space Flight Dynamics, Pasadena, CA, October 2012.

[68]Schoenenberger, M., Van Norman, J., Dyakonov, A., Karlgaard, C. D., Way, D., and Kutty, P., "Preliminary Comparison of Preflight and Reconstructed Aerodynamics of the Mars Science Laboratory Entry Vehicle," AAS Paper 13-306, AAS/AIAA Space Flight Mechanics Meeting, Kauai, HI, February 2013, to appear.